Climatic and oceanic changes during the Middle-Late Ordovician transition in the Tarim Basin, NW China and implications for the Great Ordovician Biodiversification Event

Mu Liu[a,b,c], Daizhao Chen[a,b,c,*], Xiqiang Zhou[a,c], Wei Yuan[b,d], Maosheng Jiang[a,c], Lijing Liu[e]

[a] Key Laboratory of Petroleum Resources Research, Institute of Geology and Geophysics, Chinese Academy of Sciences, Beijing 100029, China
[b] University of Chinese Academy of Sciences, Beijing 100049, China
[c] Institutions of Earth Science, Chinese Academy of Sciences, Beijing 100049, China
[d] State Key Laboratory of Environmental Geochemistry, Institute of Geochemistry, Chinese Academy of Sciences, Guiyang 550002, China
[e] Department of Geology, Northwest University, Xi'an 710127, China

ABSTRACT

The Middle-Late Ordovician transition (Darriwilian to Sandbian Age) witnessed a major pulse of the Great Ordovician Biodiversification Event (GOBE) and distinctive oceanic geochemical fluctuations, such as coeval negative C and Sr isotope excursions. In this study, investigations into geochemical variations, notably the Hg abundance (or Hg/TOC), have been carried upon the organic-rich black shale of the Middle-Upper Ordovician Saergan Formation to unravel the causes of this pulse. Based on these data, three phases were identified. Phase 1 (0 to 3 m) is characterized by rising Hg/TOC (up to 138 ppb/wt%) and Ti/Al values as well as high CIA_{corr} (corrected chemical index of alteration) values (68.9–72.3) with negligible enrichment of redox sensitive elements (RSE) and nutrient elements (e.g. U ≤ 5.2 ppm, V ≤ 153 ppm, Mo ≤ 1.8 ppm, P_2O_5 ≤ 0.2%), suggesting intensified volcanism, which could have emitted significant amounts of greenhouse gases, thereby leading to climate warming. In contrast, Phase 2 (3 to 11 m) is characterized by decreasing Hg/TOC and Ti/Al ratios, relatively low though slightly fluctuating CIA_{corr} values, generally depleted in RSE (except moderately enriched U up to 14.6 ppm) and increased P/Al and Ba/Al ratios, implying weakening volcanic activity and subsequent climate cooling and the potential for improved seawater ventilation as a result of oceanic upwelling. Phase 3 (Sandbian Age: 11–13 m) witnessed continuous decrease in Hg/TOC ratio, an increase in Ti/Al and CIA_{corr} values, fairly low values of RSE enrichment and P/Al and Ba/Al ratios, indicating recurrent climate warming, and the potential for slowed oceanic circulation and attenuated upwelling of nutrient-rich deep waters onto the shallow shelf. These changes could have diminished bioproductivity and organic output onto the seafloor. This study offers insights into volcanic-climatic-oceanic interactions during a major pulse of the GOBE around the Middle-Late Ordovician transition while black shales were extensively deposited.

1. Introduction

The Ordovician is a critical period with distinct changes in Earth's atmosphere, hydrosphere, and biosphere. Particularly, a significant and rapid diversification of marine organisms through the Ordovician, known as the Great Ordovician Biodiversification Event (GOBE), is one of the two most significant evolutionary events in the Phanerozoic (Webby et al., 2004; Harper, 2006; Servais et al., 2010; Rasmussen et al., 2016; Servais and Harper, 2018). Interestingly, the GOBE is also marked by a diversification pulse of the benthic community during the

late Middle-early Late Ordovician (Darriwilian to Sandbian Age) interval (Sepkoski, 1981; Harper, 2006; Servais and Harper, 2018). However, only a few studies have focused on this major pulse in spite of significant coeval environmental perturbations (Rasmussen et al., 2016). The Middle-Late Ordovician transition witnessed distinct geochemical fluctuations, such as MDICE (Middle Darriwilian δ^{13}C isotope excursion; Albanesi et al., 2013; Sial et al., 2013b) and a drop in seawater ^{87}Sr/^{86}Sr ratio during the Darriwilian (Qing et al., 1998; Shields et al., 2003; Edwards et al., 2015; Kah et al., 2016), which have been proposed to be induced by enhanced mafic volcanic activity (Young

---

et al., 2009), marine redox change (Young et al., 2016), intensified chemical weathering or climatic variations (Edwards and Saltzman, 2016; Saltzman and Edwards, 2017). Although studies have proved that the Middle-Late Ordovician transition (Darriwilian to Sandbian Age) could provide a useful time span to explore and understand the co-evolution of life and environment during the major pulse of GOBE (Schmitz et al., 2010; Munnecke et al., 2011; Smith et al., 2011; Algeo et al., 2016), the relationship between coeval volcanic intensity and oceanic changes has not been investigated yet. Hg concentrations have been utilized in a number of studies to investigate the link between major environmental perturbations and intensified volcanism (see references in Percival et al., 2018). By using Hg concentrations as a volcanic tracer, the volcanic intensity during the Middle-Late Ordovician transition could be suggested.

Coincident with the major pulse of the GOBE, organic-rich shales were widely deposited in multiple continents during the Middle-Late Ordovician transition, such as the Athens Shale in North America (Bergström et al., 2000), Dicellograptus Shale in Sweden (Bergström et al., 2000), Hanadir Shale in Saudi Arabia (Strother et al., 1996), Cyffredin Shale in Wales (Lev et al., 1998), Miaopo Shale in South China (Munnecke et al., 2011; Ma et al., 2015), as well as the Saergan Shale in Tarim Basin, northwestern China (Zhang and Munnecke, 2016; Chen, 2017). The deposition of organic-rich shales is generally favored by anoxic and/or nutrient-rich environment (Legget et al., 1981; Meyer and Kump, 2008). The coincidence of widespread shale deposits and the major pulse of the GOBE during Middle-Late Ordovician transition implicate the oceanic environment variations played important role in this biodiversification event. In this light, the palaeo-climatic and -oceanic conditions while the Middle-Upper Ordovician black shales were deposited and their relationships with the major pulse of GOBE deserve further investigation.

Black shale of the Saergan Formation is well exposed at the Dawangou section in the Aksu area, northwestern Tarim Basin of China. Based on detailed biostratigraphic studies, this section spans the Middle-Upper Ordovician boundary, and has been selected as a global auxiliary stratotype for the base of the Upper Ordovician (Bergström et al., 2000; Zhen et al., 2011; Chen et al., 2012; Bergström et al., 2017; Chen et al., 2017), which is ideal for study of chemostratigraphy. Here we present a comprehensive geological and geochemical study of the Saergan Shale to elucidate depositional environment, seawater redox state, paleoproductivity, climate and potential volcanism by facies observation, and geochemical analysis on major and trace element, including mercury abundance. This study provides important environmental implications for understanding the major pulse of the GOBE.

2. Geological setting

The Tarim Basin is one of the largest inland petroliferous basins on the oldest continental blocks in China ($56 \times 10^4 \, \text{km}^2$; Fig. 1B; Graham et al., 1990; Xu et al., 2011). During the Ordovician, the Tarim Block was generally composed of three (Northern, Central and Southern) uplifts and four (Kuqa, Northern, Southwestern and Southeastern) depressions (Fig. 1C; Jia et al., 2004; Lin et al., 2012). The Dawangou section (40°43.292′N, 79°32.248′E), was palaeogeographically located in the basinal setting at the western end of the Central Uplift of the Tarim Basin (Fig. 1B; Zhang and Munnecke, 2016). Based on the affinity of chitinozoan, conodont and graptolite fossils, the Tarim Basin was likely close to North China and Siberia during Middle-Late Ordovician transition (Fig. 1A; Chen et al., 2006; Torsvik and Cocks, 2013).

At Dawangou section, the Middle Ordovician to Silurian succession is continuously exposed and includes the Dawangou, Saergan, Kanling, Yingan and Terekawat formations in ascending order. The Saergan Formation comprises a 13 m-thick thin-bedded black shale succession intercalated with carbonate nodules locally (Fig. 2B), bearing abundant graptolite, acritarch, and chitinozoan fossils (Chen et al., 2012). There are four graptolite zones (the *Pterograptus elegans*, the *Didymograptus*

murchisoni, the *Dicellograptus vagus*, and the *Nemagraptus gracilis* biozones in ascending order) and two synchronous conodont biozones (the *Pygodus serra* and the *Pygodus anserinus* biozones), which consistently suggests a time span from middle Darriwilian to early Sandbian Age (Zhen et al., 2011; Chen et al., 2012; Bergström and Ferretti, 2017). Detailed biostratigraphy and the first appearance datum (FAD) of the graptolite *N. gracilis* suggest the base of the Upper Ordovician is 2 m below the top of the Saergan Formation at the Dawangou section (Fig. 2A) as an auxiliary GSSP (Global Boundary Stratotype Section and Point; Bergström et al., 2000). The Saergan Formation conformably overlies the Dawangou Formation, which is composed of grey medium-bedded, nodular bioclastic limestones (Fig. 2C) and is overlain by the Kanling Formation (Fig. 2A), which consists of nodular limestones and purplish red, thin-bedded, nodular limestones.

The Saergan Formation is composed of alternating laminae of fine-grained, organic-rich and coarser-grained, more organic-poor couplets (Fig. 3A), in which benthic fauna (i.e., trilobite, Fig. 3B) and pelagic fauna (i.e., nautiloid and radiolarian; Fig. 3C and D) are commonly observed. Changes in lithology and faunal assemblages through the section suggest a transgressive sequence (Zhao et al., 2017), which is consistent with the eustatic pattern from the Middle to the early Late Ordovician (Haq and Schutter, 2008).

3. Methods

3.1. Analytical methods

For TOC analyses, 200 mg aliquots of sample were first treated twice with 10% by volume hydrochloric acid (HCl) at 60 °C for 12 h to remove carbonate completely. Samples were then washed with distilled water to remove HCl and dried overnight (50 °C) before being weighed. Finally, Euro-EA3000 elemental iianalyzer was used to obtain TOC data at the Institute of Geology and Geophysics, Chinese Academy of Sciences (IGGCAS).

X-ray fluorescence spectrometry (XRF) was used to determine select major (Al, Ca, Fe, K, Mg, Mn, Na, P, Si and Ti). In order to determine the loss on ignition (LOI), 500 mg of pulverized sample was oxidized at 1000 °C for 1 h then cooled and thoroughly mixed with 5000 mg of lithium borate (mixture of 67% $\text{Li}_2\text{B}_4\text{O}_7$ and 33% anhydrous LiBO_2). Fusion glass disks were made by melting the mixtures at 1200 °C. The final analysis was performed using an AXIOS Minerals (PANalytical) spectrometer at the IGGCAS. The gas carrier is helium with a flow of 180 ± 10 ml/min. The pressure of carrier is 110 kPa. Oxidation time is 8.8 s and sample delay time is 5 s. The standards used in this regard are atropine sulphate (C, 58.75%; H, 7.25%; N, 4.03%; O, 25.33%; S, 4.61%). The detection limit was calculated as the concentration of analyte that corresponds to three times the standard deviation of twelve replicate measurements of the procedural blank sample using the entire sample treatment process (LOD = 3σ, where σ is the standard deviation of blank determination).

Procedures of Qi et al. (2000) were used to prepare samples for trace elemental (Li, Be, Sc, V, Cr, Co, Ni, Cu, Zn, Ga, Rb, Sr, Y, Mo, Ba, Pb, Th, U and rare earth elements) analyses. Aliquots of 50 mg of each sample were first treated with mixture of 2 ml concentrated HNO_3 and 1 ml HF, then heated at 200 °C for 48 h within sealed Teflon bombs and screw top PTFE-lined stainless steel bombs. Insoluble residues were dissolved at 130 °C using 5 ml 30% (v/v) HNO_3 for 3 h and then 2 ml concentrated HCl for 10 h to achieve complete dissolution. Samples were diluted 400-fold using 2% HNO_3 and 1 ml of 1 mg/ml Rh solution was added as an internal standard. Trace elements and REE were then analyzed as the target elements on a quadrupole inductively coupled plasma mass spectrometer (ICP-MS) at the Institute of Geochemistry, Chinese Academy of Sciences (IGCAS). The analytical precision as determined by replicate analyses of consistency standards was better than 2% RSD (1σ). Analytical calibration was accomplished using aqueous standard solutions. Details of the standard reference materials see Qi
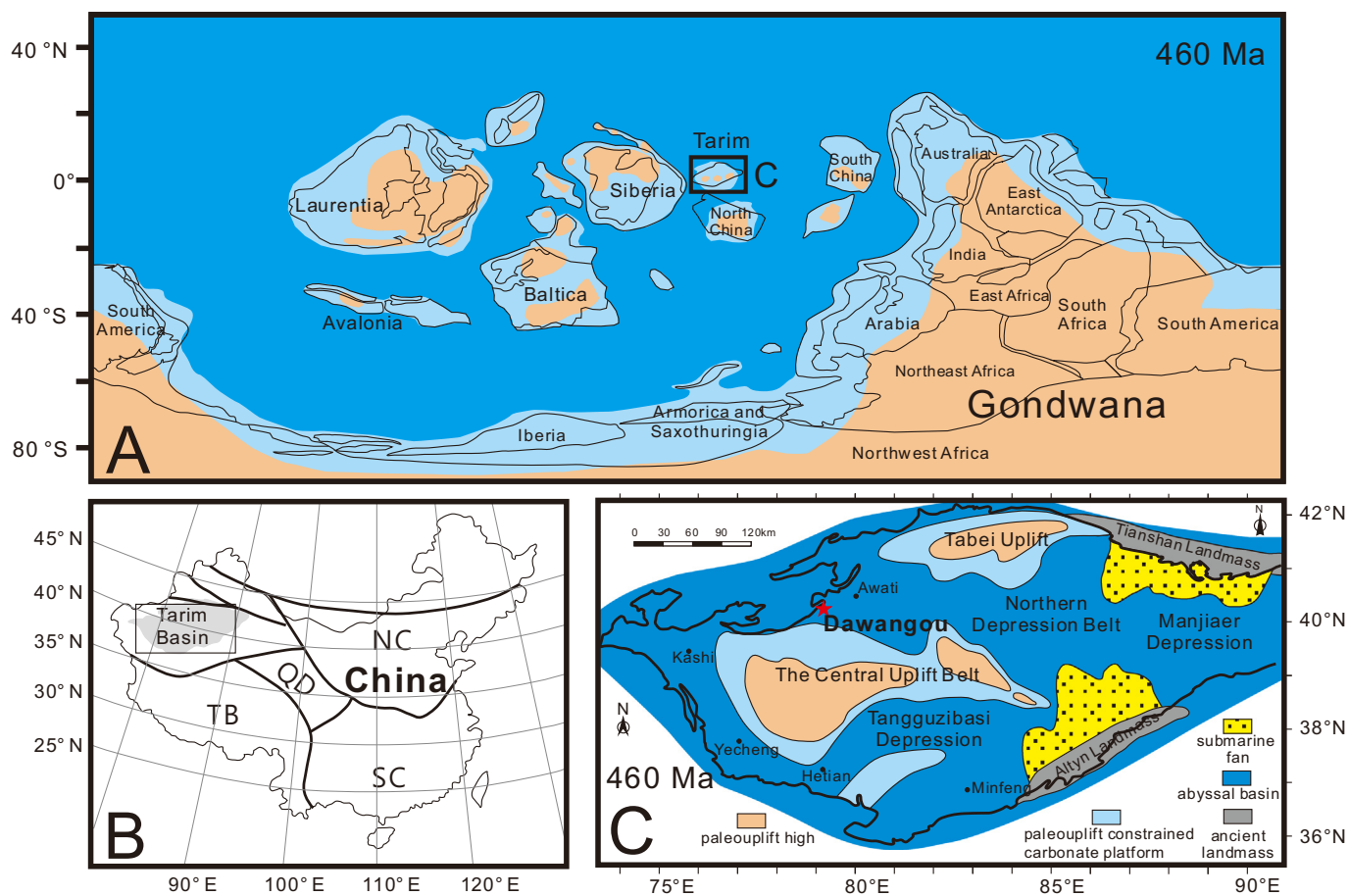
Fig. 1. A) Global palaeogeographic map showing palaeoenvironments on the continental configurations for the late Middle Ordovician (460 Ma). Note the uplands (earthy yellow), shallow-water environments (light blue) and deep-water environments (dark blue) (modified from Torsvik and Cocks (2013) and Pohl et al. (2016)). B) Major tectonic plates of the China mainland and the location of the Tarim Basin (NC = North China, SC = South China, TB = Tibet, QD = Qaidam). C) Map showing the palaeogeographic settings of the Tarim Basin in the late Darriwilian age. Note the location (red star) of the Dawangou outcrop (modified from Lin et al. (2012) and Gao et al. (2010)). (For interpretation of the references to color in this figure legend, the reader is referred to the web version of this article.)

et al. (2000).

Prior to Hg analyses, the sample powders were air-dried at 50 °C for 2 h. Hg concentrations of the samples were measured using a Lumex RA-915+ Hg analyzer equipped with a pyrolysis attachment at the IGCAS. Standards were measured after every 10 samples using GBW07405 (GSS-5) as the Hg standard, and coefficients of variation for triplicate analyses were < 6%.

3.2. Geochemical proxy calculations

3.2.1. Chemical index of alteration (CIA)

In this study, chemical index of alternation (CIA) is used to evaluate the intensity of chemical weathering for the Saergan Formation. CIA is calculated as $[Al_2O_3 / (Al_2O_3 + CaO^* + Na_2O + K_2O)] \times 100$ (Nesbitt and Young, 1982; Young and Nesbitt, 1999;). CaO^* represents CaO content in silicate fraction. CaO is first corrected for phosphate using available P_2O_5 data ($CaO^* = $ mole $CaO - $ mole $P_2O_5 \times 10 / 3$; McLennan, 1993). If the remaining amount of CaO^* is higher than Na_2O content after correction, the CaO^* is assumed to be equivalent to the Na_2O content (McLennan, 1993).

Diagenetic addition of K (K-metasomatism), which is the dominant diagenetic reaction in shales, is corrected using an Al_2O_3 - $CaO^* + Na_2O$ - K_2O (A-CN-K) ternary diagram (Fedo et al., 1995). Alternatively, the amount of diagenetic K_2O addition to each sample can be calculated using the following equation: $K_2O_{corr} = [m \times A + m \times (C^* + N)] / (1 - m)$, where $m = K /$

$(A + C^* + N + K)$ for protolith, A and $(C^* + N)$ and K are the molar values of Al_2O_3, $(CaO^* + Na_2O)$ and K_2O, respectively (Rieu et al., 2007; Panahi et al., 2000). The K-corrected CIA value is expressed as CIA_{corr}.

3.2.2. Enrichment factor (EF)

In general, the enrichment or depletion pattern of trace-element concentrations with respect to the reference material is critical to reconstruct paleoenvironmental conditions (Tribovillard et al., 2006). In order to trace the authigenic fraction of elements, normalization to an index of the detrital component, normally Al, is necessary (Francois, 1988). To make results of the normalization comparable, it is common to use enrichment factors (EF): $EF_{element\ X} = X/Al_{sample} / X/Al_{standard}$ (Calvert and Pedersen, 1993; Morford and Emerson, 1999; Piper and Perkins, 2004). If EF_X is > 1, then element X is enriched relative to standard shale; if EF_X is < 1, it is depleted (Tribovillard et al., 2006). In this study, the post-Archean Australian Shale (PAAS) geochemical data are used as $Al_{standard}$ (Taylor and McLennan, 1985).

4. Results

4.1. Major elements

Major element contents of the Saergan Shale are listed in Table 1. Consistent with petrographic analyses, the Saergan Shale is mainly composed of SiO_2 (43.7%–81.1%), relatively high CaO (up to 19.3%),
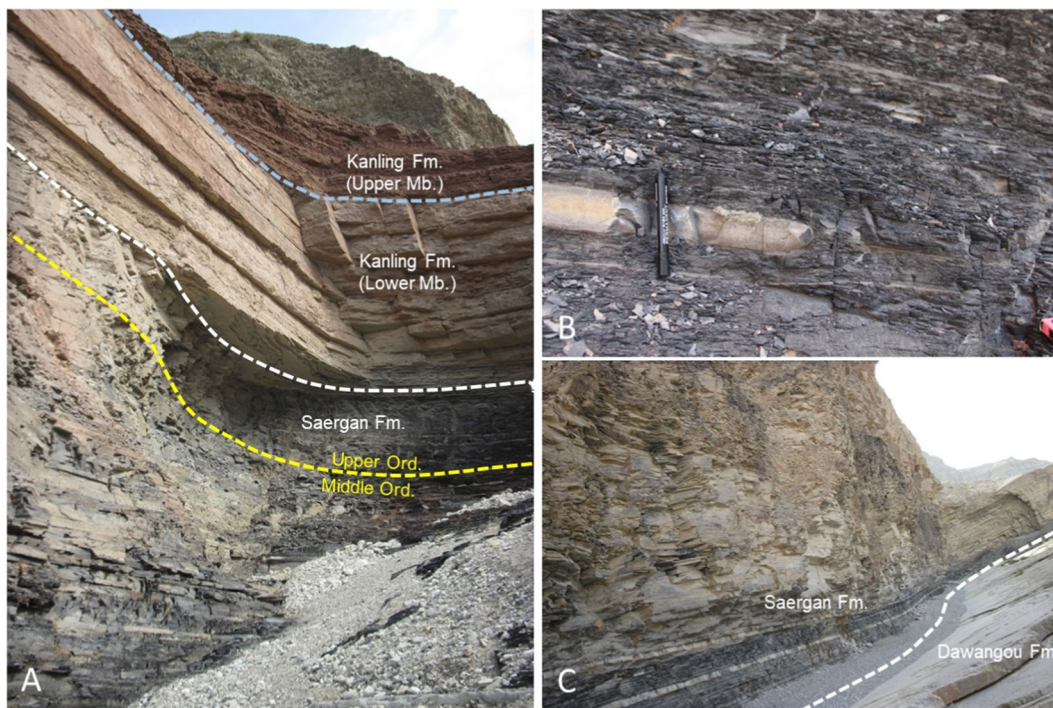
Fig. 2. Field photos of the Dawangou section, Kalping area, Tarim basin. A) Boundary between the limestone of Kanling Formation and black shale of Saergan Formation. The auxiliary GSSP for the base of the Upper Ordovician is located ~2 m below the top of the Saergan Formation. B) Black shale with carbonate nodules in the Saergan Formation. C) Panoramic view on the vertical succession from well-bedded limestone of the Dawangou Formation to the black shale of the Saergan Formation (Fm. = Formation, Ord. = Ordovician).

Fig. 3. A) Horizontal fine lamination illustrated by organic-rich and -poor (silty quartz) layers; B) Trilobite fragment in organic-rich shale; C) Thin-shelled clasts (nautiloids?) bedded parallelly in the organic-rich shale; D) Abundant siliceous radiolarian in shale.

Table 1

Total organic carbon (TOC), mercury and major element concentration of the Saergan Formation at Dawangou section, Tarim Basin, Northwestern China.

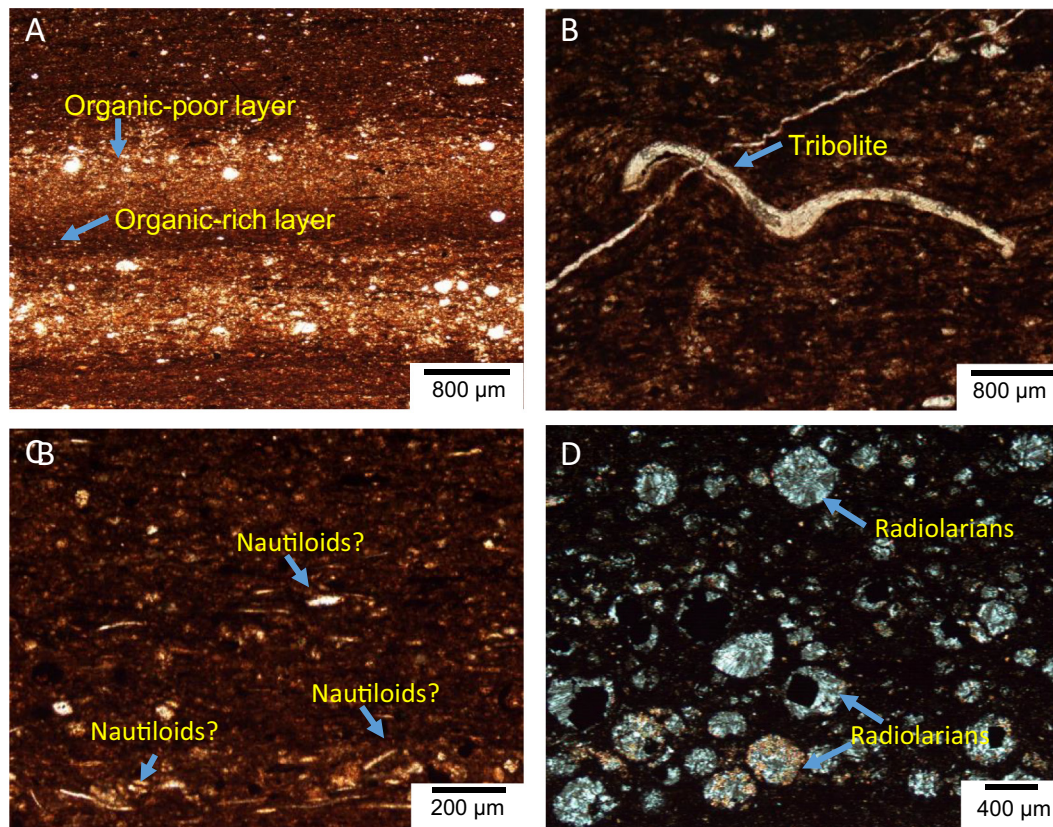| Sample no.	Height (m)	TOC wt%	Hg (ppb)	SiO$_2$ (%)	TiO$_2$ (%)	Al$_2$O$_3$ (%)	TFe$_2$O$_3$[a] (%)	MnO (%)	MgO (%)	CaO (%)	Na$_2$O (%)	K$_2$O (%)	P$_2$O$_5$ (%)	LOI[b] (%)	Total (%)
1	0.30	4.79	71	49.1	0.66	13.7	3.31	0.02	2.11	9.66	0.58	4.73	0.22	15.8	99.9
2	0.60	2.12	103	63.3	0.63	12.4	3.82	0.01	2.17	4.33	0.48	4.21	0.14	8.34	99.8
3	0.90	1.93	90	62.7	0.66	13.4	3.80	0.01	2.35	3.54	0.48	4.64	0.14	7.74	99.4
4	1.20	1.57	138	59.0	0.72	14.0	4.17	0.02	2.68	5.15	0.58	4.86	0.11	8.59	99.8
5	1.50	0.54	65	63.1	0.55	10.1	3.46	0.02	2.31	7.47	0.48	3.29	0.21	8.66	99.7
6	2.00	0.54	75	56.8	0.66	11.9	3.89	0.02	2.54	8.73	0.58	4.03	0.14	10.1	99.4
7	2.35	2.94	224	53.2	0.64	12.4	4.14	0.02	2.24	7.76	0.63	4.23	0.23	13.7	99.1
8	2.85	1.83	238	50.8	0.59	11.2	4.21	0.02	2.23	12.2	0.58	3.79	0.20	13.7	99.4
9	3.25	2.68	237	62.8	0.46	8.96	3.44	0.02	1.67	7.68	0.58	2.93	0.15	10.7	99.4
10	3.55	1.71	168	51.4	0.36	6.78	2.34	0.02	1.41	18.0	0.47	2.18	0.48	16.2	99.7
11	3.85	1.86	139	60.8	0.44	8.08	2.35	0.02	1.59	10.8	0.57	2.55	1.02	11.3	99.4
12	4.13	3.30	263	59.8	0.42	8.23	2.46	0.02	1.40	10.5	0.62	2.73	1.15	12.4	99.5
13	4.33	2.19	166	65.7	0.32	6.28	1.90	0.02	1.21	9.97	0.50	1.99	0.24	11.7	99.8
14	4.63	1.78	193	66.9	0.35	6.98	2.43	0.02	1.26	8.69	0.50	2.27	0.19	9.80	99.4
15	5.23	1.48	93	54.1	0.24	4.90	1.53	0.03	0.98	19.3	0.48	1.43	0.43	16.5	99.9
16	5.53	2.16	142	70.6	0.30	5.93	1.71	0.01	1.14	8.09	0.50	1.83	0.73	8.67	99.5
17	5.63	1.40	155	61.4	0.46	8.99	2.89	0.02	1.55	9.95	0.59	2.82	0.82	10.3	99.8
18	6.23	2.84	192	67.5	0.46	9.12	2.64	0.02	1.43	6.12	0.66	2.89	0.41	8.69	99.9
19	6.53	1.52	125	81.1	0.20	3.96	1.56	0.01	0.83	4.67	0.39	1.16	0.16	5.94	100.0
20	7.13	2.00	161	62.2	0.50	10.0	2.83	0.01	1.45	8.12	0.65	3.13	1.61	8.75	99.3
21	7.73	3.01	185	70.5	0.38	7.78	2.10	0.02	1.21	5.88	0.62	2.43	0.72	8.38	100.0
22	7.93	2.77	185	58.8	0.49	9.84	2.70	0.02	1.79	9.58	0.72	3.17	2.08	10.2	99.4
23	8.33	4.54	288	53.6	0.59	12.0	3.18	0.03	2.21	9.11	0.94	3.74	0.80	13.2	99.4
24	8.73	4.27	290	46.9	0.54	11.1	3.44	0.03	2.16	14.1	0.90	3.46	1.06	15.8	99.5
25	9.23	4.49	338	49.2	0.55	11.6	4.16	0.03	2.12	11.0	0.88	3.65	2.28	13.9	99.3
26	9.73	2.53	135	50.6	0.61	12.7	3.74	0.03	2.32	11.4	0.84	4.06	0.16	13.6	100.0
27	10.13	4.33	187	48.4	0.59	12.5	3.66	0.03	2.14	12.0	0.90	3.89	1.38	14.0	99.4
28	10.43	4.33	266	43.7	0.54	11.4	4.16	0.03	1.97	14.5	0.92	3.44	2.17	16.9	99.6
29	10.73	2.74	62	51.5	0.64	13.1	3.41	0.04	2.44	10.1	0.85	4.26	0.26	12.7	99.3
30	11.03	1.53	65	50.0	0.67	13.4	3.54	0.04	2.40	11.2	0.73	4.46	0.16	13.0	99.6
31	11.43	2.35	47	47.9	0.64	13.2	3.46	0.04	2.38	12.7	0.73	4.46	0.14	14.5	100.1
32	11.93	2.40	37	48.0	0.65	13.3	3.50	0.04	2.40	12.0	0.75	4.48	0.15	14.0	99.3

[a] TFe$_2$O = total iron concentrations.

[b] LOI = loss on ignition.

moderate Al$_2$O$_3$ (3.9%–13.7%), and minor Fe$_2$O$_3$ (1.9%–4.2%) and MnO (0.01%–0.04%). P$_2$O$_5$ ranges between 0.1%–2.3%. TOC ranges from 0.5 wt% to 4.8 wt%, (averages 2.51 wt%). High TOC samples (> 4.0 wt%) are located approximately 9–10 m from the base of the Saergan Formation, close to the boundary of *D. murchisoni* and *N. gracilis* graptolitic biozone (Fig. 4).

The effects of K metasomatism can be corrected by projecting each data point back to its original (predicted) position on the A–CN–K ternary diagram (Fig. 5; Fedo et al., 1995). CIA$_{corr}$ values, calculated using major element abundances, cluster from 60.6 to 72.4. At the basal Saergan Formation, CIA$_{corr}$ values are relatively higher (~71; Fig. 4) then the CIA$_{corr}$ values decrease upwards, displaying a negative excursion (down to 60.64) though fluctuating. At approximately 11 m from the base (around the start of the Upper Ordovician), CIA$_{corr}$ values start to increase to ~68 until the top. Uncorrected CIA values are generally lower than CIA$_{corr}$ values (from 61.0 to 67.0), but display similar variation patterns (Fig. 4).

Between 0 and 3 m P/Al values are low (< 0.02) and vary little. Between 3 and ~11.5 m, values increase to a maximum values of 0.17 and vary widely between 0.03 and 0.17. Between ~11.5 m and the top of the section, values return to ~0.01 and vary little.

4.2. Trace elements

Trace element concentrations and enrichment factors are shown in Tables 2 and 3, respectively. Generally, trace elements display slight enrichment with respect to PAAS. Enrichment factors of V and Mo (EF$_V$ and EF$_{Mo}$) are slightly high, ranging between 1.6–4.9 and 0.8–25.2, respectively. In contrast, U is the most enriched (EF$_U$ up to 49.2). Furthermore, Mo/TOC (ppm/wt%) ranges from 0.15 to 1.84 (average 0.66). Vertically, these elements are more enriched in middle part

compared with those in the basal and uppermost part of the section. Micronutrients such as Ni, Cu, and Zn show enrichment factors (EF$_{Ni}$, EF$_{Cu}$, and EF$_{Zn}$) ranging from 1.4–6.1, 2.4–8.5, and 1.3–10.9, respectively. The enrichment factor for Ba is generally low (average 1.7). Ti/Al values rise (0.055–0.063) between 0 and ~2.5 m, then decrease episodically from 0.063 to 0.053 between ~2.5 and ~11.5 m. Between ~11.5 m and the top of the Saergan Formation, Ti/Al values fluctuate between 0.053 and 0.056 (Fig. 4).

4.3. Mercury abundance

In the basal section (0–2 m), the Hg abundance is relatively low (65–138 ppb). Hg abundance is episodically fluctuating between 2 and 11 m, generally following the TOC variation pattern in the Saergan Formation (Fig. 4). A negative excursion of Hg abundance is observed at the interval between 4.5 and 8 m. In comparison, the Hg/TOC (ppb/wt%) values show an apparent increase to a maximum of 138 in the lower part of the Saergan Formation, and then decline through the rest of the section.

5. Discussion

Before detailed interpretation, the Saergan Formation is subdivided into three phases based on variation of geochemical parameter patterns. Phase 1 (0–3 m) is characterized as an interval with low Hg abundance (minimum to 65 ppb), negligible enrichment of redox sensitive (RSE) and nutrient elements (e.g. U ≤ 5.2 ppm, V ≤ 153 ppm, Mo ≤ 1.8 ppm, P/Al ≤ 0.02). In the Phase 1, Hg/TOC values increase from 14.7 to 138.4 ppb/wt%, Ti/Al values increase from 0.055 to 0.063, the CIA$_{corr}$ values decrease from 72.4 to 65.3. In Phase 2, the Hg abundance is relatively higher (up to 338 ppb), the U moderately enriched (up to
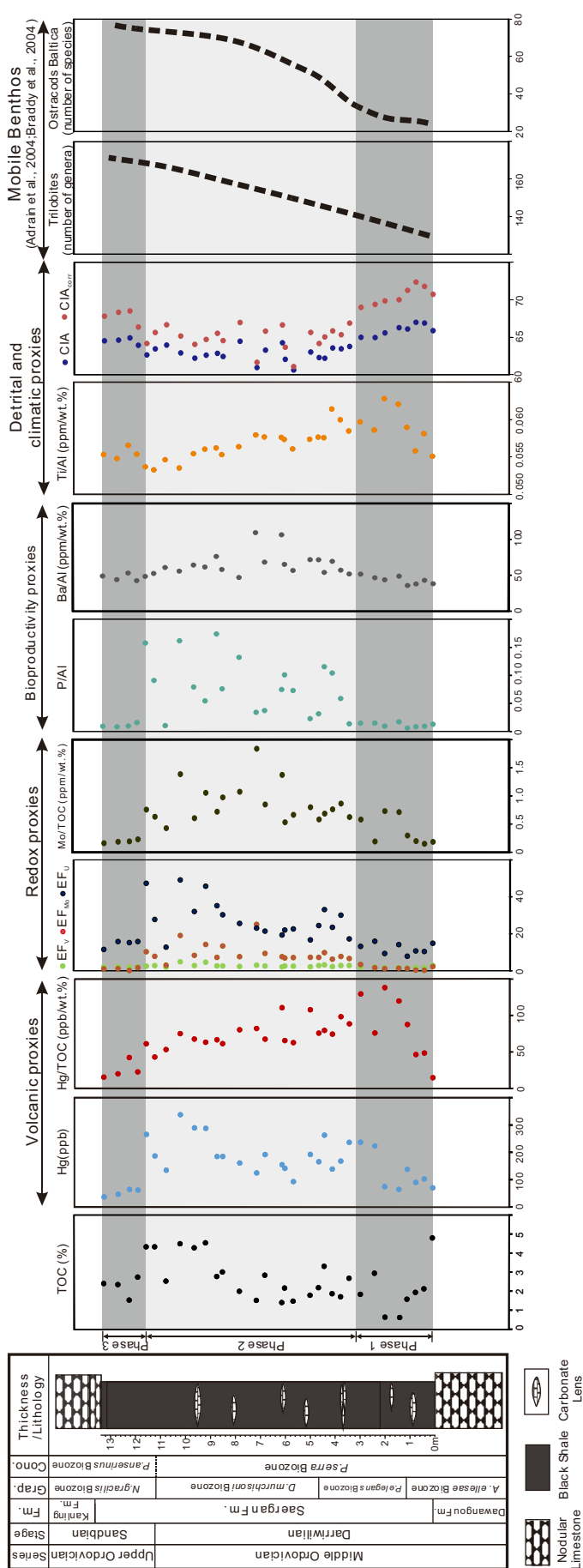
Fig. 4. The vertical distribution of TOC, mercury abundance, and other proxies of redox, productivity and climate change in the Saergan Formation from the Dawangou section along with coeval benthic diversity (Fm. = Formation, Grap. = Graptolite, Cono. = Conodont, EF = Enrichment factor). Benthic diversity data from Adrain et al. (2004) and Braddy et al. (2004).
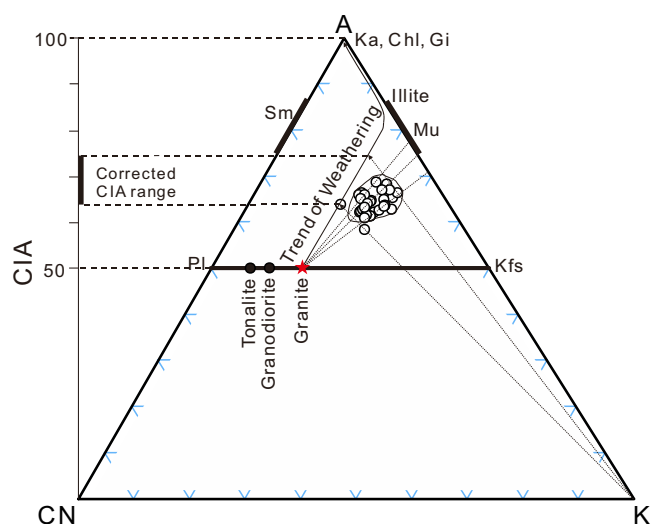
Fig. 5. A–CN–K ternary diagram of the studied samples, using the method described by Nesbitt and Young (1982). Tonalite, granodiorite, and granite data are from Condie (1993). CIA–Chemical Index of Alteration, A–Al$_2$O$_3$, CN–CaO* + Na$_2$O, K–K$_2$O (all in molar proportions), CaO*–CaO incorporated in the silicate fraction of the sample, Pl–plagioclase, Kfs–K-feldspar, Sm–smectite, Ka–kaolinite, Gi–gibbsite, Chl–chlorite, Mu–muscovite.

14.6 ppm) and CIA$_{corr}$ values remain low relatively to Phase 1. In addition, both Hg/TOC and Ti/Al values decrease in Phase 2 and P/Al and Ba/Al ratios are higher than those in Phase 1. Phase 3 (Sandbian Age; 11–13 m) witnessed continuous decrease of Hg/TOC ratios and increase of Ti/Al and CIA$_{corr}$ values, low RSE abundance, and P/Al and Ba/Al ratios.

5.1. Hg anomalies and Darriwilian volcanism

Mercury (Hg) has been shown to be a valuable proxy to trace specific geological process, particularly the volcanism (Pyle and Mather, 2003; Gustin et al., 2008). On pre-anthropogenic Earth, volcanism was the most efficient natural source of Hg to the atmosphere which could be deposited in seawater (Pirrone et al., 2010). It then could be scavenged and transported to the seafloor via organic matter deposition, resulting in a positive correlation between Hg abundance and TOC (Sanei et al., 2012; Grasby et al., 2013; Sial et al., 2013a). However, the origin of Hg anomalies should be carefully evaluated since Hg abundance in sediments can be affected by a number of factors, including sedimentation hiatus, lithological changes, extremely low TOC content, and enhanced Hg-adsorption by sulphides and clay complexes (Gustin et al., 2008; Font et al., 2016; Jones et al., 2017; Scaife et al., 2017). The Saergan Formation is dominated by black shales and calcareous shales generally rich in organic matter (Fig. 4), without distinct sedimentation hiatus and lithological change. Furthermore, high abundances of Hg (> 70 ppb) are found in samples with moderate TOC contents (> 0.5 wt%, criteria following Jones et al., 2017), suggesting Hg concentration was not entirely controlled by the rate of organic matter deposition. In addition, Hg and Al concentrations are poorly correlated (Fig. 6A), indicating Hg concentration was likely not controlled by clay deposition. Moreover, enrichment patterns of U, Mo, and V (Fig. 4) clearly suggest suboxic conditions during the Saergan shale deposition (see Section 5.3), excluding enhanced Hg-adsorption by sulphides as a mechanism for high Hg concentration. Therefore, the elevated mercury abundance in this formation is likely resulted from enhanced atmospheric Hg input via large-scale volcanism (Gustin et al., 2008).

In addition, Hg/TOC values are generally comparable to those from sediments of well-known critical geological events (Fig. 7), such as the five mass extinction events (Sanei et al., 2012; Grasby et al., 2013; Sial

Table 2
Selected trace element concentration of the Saergan Formation at Dawangou section, Tarim Basin, Northwestern China.

Sample no.	Height (m)	V (μg/g)	U (μg/g)	Mo (μg/g)	Cr (μg/g)	Co (μg/g)	Ni (μg/g)	Ba (μg/g)	Cu (μg/g)	Zn (μg/g)	Th (μg/g)	Zr (μg/g)	Cd (μg/g)	Sc (μg/g)
1	0.30	153.2	5.2	0.9	90.1	38.5	127.5	276.4	157.8	38.7	14.0	142.8	0.06	10.6
2	0.60	91.1	3.3	0.3	58.8	13.4	62.6	282.6	93.6	92.0	14.6	116.3	0.08	11.5
3	0.90	100.4	3.7	0.4	62.1	11.0	59.2	269.1	99.5	95.8	16.8	140.2	0.12	11.2
4	1.20	84.7	2.8	0.5	63.3	11.8	46.3	264.8	100.1	116.1	15.3	124.3	0.13	11.5
5	1.50	68.6	3.6	0.4	48.5	6.2	21.7	260.3	53.5	143.8	10.0	97.4	0.12	10.5
6	2.00	76.4	2.9	0.4	53.5	8.1	26.4	276.0	39.9	60.2	12.1	111.8	0.08	9.5
7	2.35	99.6	5.1	0.6	69.8	15.7	81.8	304.2	123.0	301.9	14.2	115.2	0.20	11.3
8	2.85	85.2	3.8	1.1	57.2	11.5	59.2	305.1	81.0	95.1	11.5	100.6	0.08	10.0
9	3.25	101.0	3.9	1.7	53.1	7.8	60.1	245.6	89.6	85.4	9.5	84.1	0.07	8.7
10	3.55	75.1	5.2	1.5	34.0	7.7	38.3	204.8	63.8	63.4	6.5	63.0	0.07	7.1
11	3.85	72.1	4.8	1.4	46.2	6.7	41.7	296.8	68.8	63.0	8.6	79.9	0.04	9.0
12	4.13	103.8	6.9	2.3	54.3	8.9	76.2	234.7	98.1	102.7	6.8	77.8	0.09	8.9
13	4.33	69.8	3.9	1.3	46.0	6.7	43.7	237.8	61.5	93.4	7.8	59.0	0.04	6.8
14	4.63	59.9	3.0	1.4	41.3	8.6	46.8	264.9	57.2	58.3	8.3	63.9	0.03	6.4
15	5.23	48.1	2.8	1.0	34.1	4.2	28.7	146.9	47.1	41.9	5.4	45.5	0.04	4.5
16	5.53	60.0	3.3	1.2	37.9	4.8	40.7	204.4	62.5	48.3	7.3	57.2	0.05	5.7
17	5.63	73.4	4.4	1.9	43.7	7.0	35.4	506.3	49.4	103.3	9.4	82.0	0.07	8.7
18	6.23	92.0	5.0	2.4	59.5	6.7	56.3	329.3	90.6	82.2	11.4	83.4	0.07	8.5
19	6.53	47.4	2.3	2.8	121.8	4.5	32.1	229.1	40.9	40.2	4.9	35.1	0.03	4.2
20	7.13	92.9	6.6	2.2	52.9	7.2	50.8	249.0	85.6	69.3	9.7	86.5	0.08	9.7
21	7.73	80.6	6.0	2.9	46.1	6.1	50.5	239.2	66.9	65.6	9.1	72.4	0.07	8.5
22	7.93	103.0	8.8	2.0	56.8	7.0	54.7	396.7	85.5	102.0	7.5	87.5	0.07	10.0
23	8.33	218.9	14.0	4.8	80.5	8.7	85.9	390.4	100.0	136.0	11.2	114.1	0.23	10.6
24	8.73	123.1	9.1	2.6	62.9	10.6	79.4	376.0	95.4	111.3	11.0	102.9	0.05	9.2
25	9.23	222.0	14.6	6.2	81.6	12.2	96.5	342.8	108.1	157.7	6.7	111.7	0.17	11.2
26	9.73	98.5	4.1	1.1	63.6	12.0	61.6	409.2	89.9	110.6	11.5	116.2	0.09	10.3
27	10.13	139.3	8.8	2.7	77.0	10.4	81.3	346.9	114.2	171.1	11.0	111.7	0.11	10.1
28	10.43	112.4	13.7	3.3	61.9	16.2	90.2	290.5	91.8	123.1	6.7	103.8	0.11	9.4
29	10.73	112.7	5.3	0.6	64.3	10.9	51.3	295.6	78.0	128.3	9.4	119.5	0.11	8.7
30	11.03	106.5	5.2	0.3	62.5	12.1	41.0	376.9	67.3	89.7	9.8	123.0	0.05	9.3
31	11.43	115.9	5.3	0.4	63.9	15.1	54.9	307.8	84.7	125.6	9.8	127.0	0.15	9.6
32	11.93	108.7	3.9	0.4	61.1	10.3	50.5	345.1	97.2	93.0	10.4	127.3	0.10	7.8

Table 3

Essential inter-element ratios and element proxies of the Saergan Formation at Dawangou section, Tarim Basin, Northwestern China.

Sample no.	Height (m)	Hg/TOC (ppb/wt%)	P/Al	Ba/Al × 10⁻⁴	Ti/Al	CIA	CIA$_{corr}$	EF$_{Ni}$[a]	EF$_{Cu}$	EF$_{Zn}$	EF$_V$	EF$_{Mo}$	EF$_U$	Mo/TOC × 10⁻⁴
1	0.30	14.7	0.01	38.2	0.055	66.0	70.9	6.1	8.2	1.3	2.9	2.3	14.9	0.18
2	0.60	48.6	0.01	43.0	0.058	66.9	71.8	3.3	5.4	3.3	1.9	0.9	10.4	0.15
3	0.90	46.6	0.01	37.9	0.058	67.0	72.4	2.9	5.3	3.1	1.9	1.0	10.8	0.20
4	1.20	87.7	0.01	35.8	0.059	66.1	71.3	2.2	5.1	3.7	1.6	1.2	7.9	0.30
5	1.50	120.0	0.02	48.7	0.062	66.3	70.0	1.4	3.8	6.4	1.7	1.4	14.2	0.71
6	2.00	138.4	0.01	43.7	0.063	65.6	69.8	1.4	2.4	2.3	1.6	1.2	9.4	0.73
7	2.35	76.1	0.02	46.5	0.058	65.0	69.3	4.3	7.1	10.9	2.1	1.6	16.0	0.19
8	2.85	129.7	0.02	51.6	0.060	65.0	68.9	3.4	5.2	3.8	1.9	3.4	13.3	0.58
9	3.25	88.5	0.01	51.8	0.058	63.8	66.9	4.4	7.1	4.3	2.9	6.7	17.2	0.62
10	3.55	98.5	0.06	57.1	0.060	63.5	65.3	3.7	6.7	4.2	2.8	7.8	30.1	0.86
11	3.85	74.6	0.10	69.4	0.061	63.6	65.9	3.4	6.1	3.5	2.3	6.3	23.5	0.76
12	4.13	79.7	0.12	53.9	0.057	62.2	65.0	6.0	8.5	5.6	3.2	9.8	33.1	0.69
13	4.33	75.9	0.03	71.5	0.058	62.3	64.2	4.5	7.0	6.6	2.8	7.3	24.5	0.58
14	4.63	108.0	0.02	71.7	0.057	63.0	65.7	4.4	5.9	3.7	2.2	7.2	16.7	0.80
15	5.23	63.0	0.07	56.6	0.056	61.1	60.6	3.8	6.9	3.8	2.5	7.2	22.7	0.66
16	5.53	65.7	0.10	65.1	0.057	62.1	63.7	4.5	7.5	3.6	2.6	6.9	22.0	0.53
17	5.63	110.9	0.08	106.4	0.057	64.3	66.7	2.6	3.9	5.1	2.1	7.6	19.4	1.37
18	6.23	67.6	0.03	68.2	0.058	63.3	65.8	4.0	7.1	4.0	2.6	9.4	21.4	0.85
19	6.53	82.4	0.03	109.3	0.058	61.0	61.7	5.3	7.4	4.5	3.1	25.2	23.1	1.84
20	7.13	80.6	0.13	46.9	0.056	64.5	67.0	3.3	6.1	3.1	2.4	7.6	25.6	1.07
21	7.73	61.5	0.08	58.1	0.055	62.5	64.6	4.2	6.1	3.8	2.6	13.4	30.3	0.97
22	7.93	66.7	0.17	76.2	0.056	62.9	65.5	3.6	6.2	4.6	2.7	7.3	35.2	0.72
23	8.33	63.4	0.06	61.4	0.056	62.6	64.7	4.6	5.9	5.1	4.6	14.2	45.8	1.05
24	8.73	67.9	0.08	64.2	0.055	62.2	64.1	4.7	6.2	4.5	2.8	8.3	32.1	0.60
25	9.23	75.3	0.16	55.7	0.053	62.9	65.2	5.4	6.6	6.1	4.9	19.1	49.2	1.39
26	9.73	53.4	0.01	60.8	0.055	64.0	66.7	3.1	5.1	3.9	2.0	3.0	12.8	0.43
27	10.13	43.2	0.09	52.5	0.053	63.5	65.6	4.2	6.5	6.1	2.9	7.8	27.8	0.63
28	10.43	61.4	0.16	48.4	0.054	62.7	64.2	5.2	5.8	4.8	2.5	10.3	47.3	0.76
29	10.73	22.6	0.02	42.5	0.055	63.9	67.0	2.5	4.2	4.4	2.2	1.7	15.8	0.23
30	11.03	42.5	0.01	53.1	0.056	64.9	68.6	2.0	3.6	3.0	2.0	0.8	15.3	0.19
31	11.43	20.0	0.01	44.0	0.055	64.6	68.4	2.7	4.6	4.2	2.2	1.2	15.8	0.19
32	11.93	15.4	0.01	48.9	0.055	64.5	68.3	2.5	5.2	3.1	2.1	1.0	11.6	0.16

[a] EF = enrichment factor.
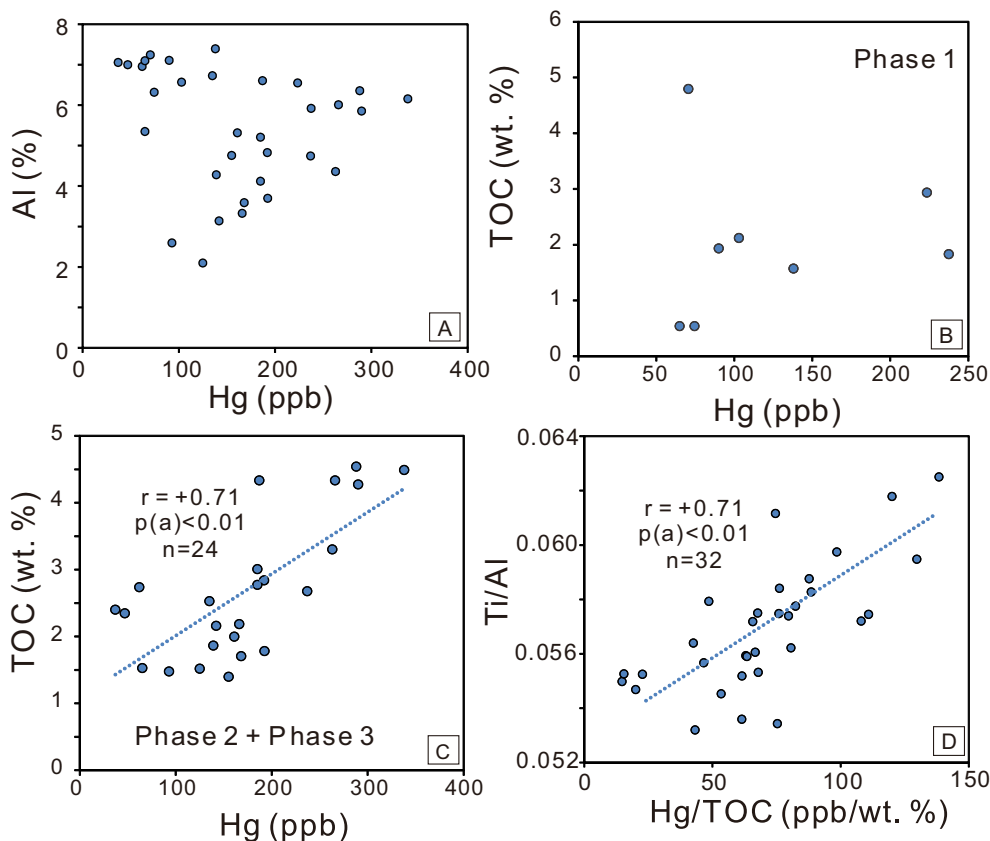
Fig. 6. A) Crossplot of Hg vs. Al; B) Crossplot of Hg vs. TOC of samples of phase 1; C) Crossplot of Hg vs. TOC of samples of Phase 2 and Phase 3; D) Crossplot of Hg/TOC vs. Ti/Al.
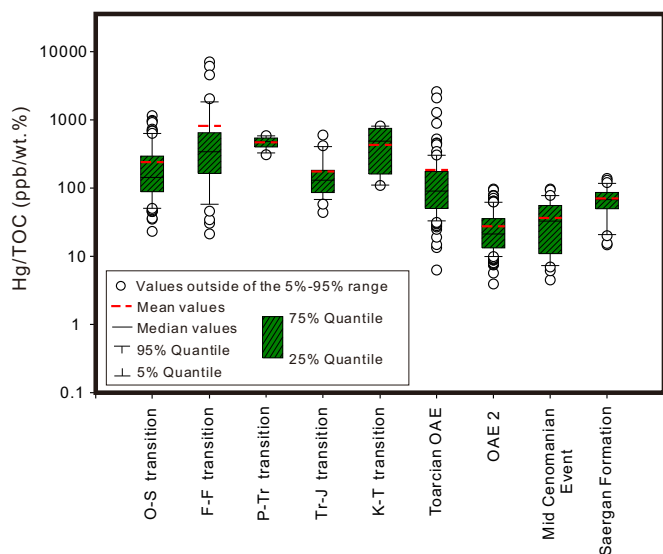
Fig. 7. Comparison of Hg/TOC (ppb/wt%) ratios from the Saergan Shale with those from other major geological events. O-S: Ordovician-Silurian; F-F: Frasnian-Famennian; P-Tr: Permian-Triassic; Tr-J: Triassic-Jurassic; K-T: Cretaceous-Paleocene; O-S data quoted from Gong et al. (2017) and Jones et al. (2017); F-F data from Racki et al. (2018); P-T data from Sanei et al. (2012), Grasby et al. (2013) and Wang et al. (2018); T-J data from Thibodeau et al. (2016); K-T data from Nascimento-Silva et al. (2011), Font et al. (2016) and Sial et al. (2013a, 2013b); Toarcian OAE data from Percival et al. (2015); OAE 2 and Mid Cenomanian Event data from Scaife et al. (2017).

et al., 2013a; Font et al., 2016; Thibodeau et al., 2016; Gong et al., 2017; Jones et al., 2017; Racki et al., 2018; Sabatino et al., 2018; Wang et al., 2018) and OAEs (oceanic anoxic events; Percival et al., 2015; Scaife et al., 2017; Charbonnier et al., 2018), which have been proposed to be related to coeval large-scale volcanism to varying extents. This further suggests intensified volcanism likely occurred during deposition of the Saergan Shale, most notably during the early stage of Phase 1, disturbing the positive correlation between Hg and TOC (Fig. 6B). Later, decreasing Hg/TOC values through Phase 2 and Phase 3 point to attenuating volcanism and the recovery of positive correlation between Hg and TOC concentrations (Fig. 6C). In addition, the positive relationship between the Hg/TOC and Ti/Al ratios (Fig. 6D) supports an increasing aeolian Hg input from volcanic eruptions since the Ti/Al ratio is a valuable proxy indicative of aeolian flux (Yarincik et al., 2000; Beckmann et al., 2005). The deposition of volcanic materials into aqueous environments would lead to dissolution of adsorbed metal salts and aerosols, increasing the bioavailability of key nutrient elements (Jones and Gislason, 2008).

The Darriwilian volcanism is also consistent with coeval geochemical records, including global sharp drop of $^{87}Sr/^{86}Sr$ (Fig. 8; Shields et al., 2003) in the late Darriwilian, which has been proposed to be linked to volcanism (Young et al., 2016). In addition, the post-MDICE negative excursion (Sial et al., 2013b; Edwards and Saltzman, 2016; Saltzman and Edwards, 2017), widespread K-bentonite beds from 450 to 470 Ma (Fig. 8; Kolata et al., 1998; Min et al., 2001; Astini et al., 2007; Huff, 2008; Thompson et al., 2012; Sell et al., 2015), large continental dispersal of the Paleozoic, rapid sea-floor spreading during the Middle Ordovician (Cocks and Torsvik, 2002; Torsvik and Cocks, 2013), and superplume activity suggested by ophiolite obduction pulses (Algeo, 1996; Vaughan and Scarrow, 2003; Barnes, 2004) further suggest the enhancement of volcanic activities during the late Darriwilian Age.

5.2. Paleoclimate conditions

The Early-Middle Ordovician epoch was characterized by a steady greenhouse climate with a long-term cooling trend, potentially facilitating the GOBE (Trotter et al., 2008). Conditions subsequently evolved into an intense icehouse climate in the Late Ordovician epoch, one of the only three major icehouse intervals in Earth's Phanerozoic (Finnegan et al., 2012). Based on the MITgcm model, the Gondwana glaciation likely started in the late Darriwilian (Pohl et al., 2016). In addition, paleontological studies suggested global cooling during Darriwilian Age (Vandenbroucke et al., 2010; Rasmussen et al., 2016; Rasumussen and Stouge, 2018). This contrasts with suggested sea surface temperature of ~30 °C based on GEOCLIM model (Nardin et al., 2011).

The CIA value of fine-grained argillites has been widely used to evaluate the relative weathering intensity and climatic background (Nesbitt and Young, 1982). Normally, CIA values higher than 70 represent clay mineral composition for warm, humid tropical climates, and cold, arid climates fall below 50 (Nesbitt and Young, 1982, 1989; Fagel, 2007). However, CIA may also be affected by provenance compositions, transport recycling, and potassium metasomatism (Fedo et al., 1995; Bahlburg and Dobrzinski, 2011), which should be evaluated prior to application.

In fine-grained siliciclastic rocks, the distribution of major and trace elements (e.g., Sc, Ti, Zr, and Th etc.) can provide valuable information on sedimentary provenance (McLennan and Taylor, 1991; Garver and Royce, 1996). Crossplots of Zr vs. TiO_2 (Hayashi et al., 1997) (Fig. 9A), La/Sc vs. Th/Co ratios (Cullers, 2002) (Fig. 9B), and ternary diagram of La–Th–Sc (Cullers and Podkovyrov, 2000) (Fig. 9C) consistently suggest that Saergan Shale derived predominantly from felsic igneous rocks. A stable provenance composition is also likely given the short duration over which the Saergan Formation deposited (< 5 Ma based on biostratigraphy and astronomical calibration; Cooper et al., 2012b; Zhong et al., 2018). Moreover, on a crossplot of Zr/Sc vs. Th/Sc ratios, data fall within the trend of the first cycle of the parent rocks (Fig. 9D), indicating limited transport recycling of their provenance rocks (McLennan, 1993, 2001).

To minimize the effect of potassium metasomatism, CIA_{corr} is used to interpret the paleo-weathering intensity and climatic patterns (Fedo et al., 1995; Bahlburg and Dobrzinski, 2011). In Phase 1 of the Saergan Formation, CIA_{corr} values are generally higher than those in Phase 2 (Fig. 4) though a gentle decreasing trend, indicating a warmer and more humid climate in Phase 1 (Fedo et al., 1995; Young and Nesbitt, 1999). This scenario is consistent with coeval high Hg/TOC ratios since enhanced volcanism may have significantly increased greenhouse gas (i.e., CO_2) releasing into the atmosphere, potentially inducing climate warming. The cooling started approximately at the late stage of Phase 1, corresponding with the shift of Hg/TOC ratios. In Phase 2, decreasing CIA_{corr} values and subsequent fluctuating around a value of 65 indicate waning weathering (or a cooling climate), likely due to the diminishing greenhouse gas venting by waning volcanic activity as evidenced by the decreasing Hg/TOC values. Although Phase 3 marked a transient recurrence of climatic warming, collectively, a transition from warm to cool climate is the general large-scale trend (Fig. 4). This transition to cooling climate may represent the prelude to Late Ordovician glaciation (Pohl et al., 2016) at least on a regional scale, which may have impacted ocean circulation, favoring upwelling, nutrient redistribution and increasing bioproductivity (Brumsack, 2006).

5.3. Marine redox environment

Redox-sensitive elements, such as Mo, V, U, are commonly used to reconstruct paleo-oceanic redox state (Piper and Calvert, 2009; Little et al., 2015; Robbins et al., 2016). To further unravel the paleo-oceanic environment, enrichment factors of selected elements in the Saergan Formation were compared with sediments from modern upwelling zones and shales deposited during Cretaceous Oceanic Anoxic Events (COAE; Fig. 10; Brumsack, 2006). It should be noted that data from Brumsack (2006) were normalized to the average shale (Wedepohl,
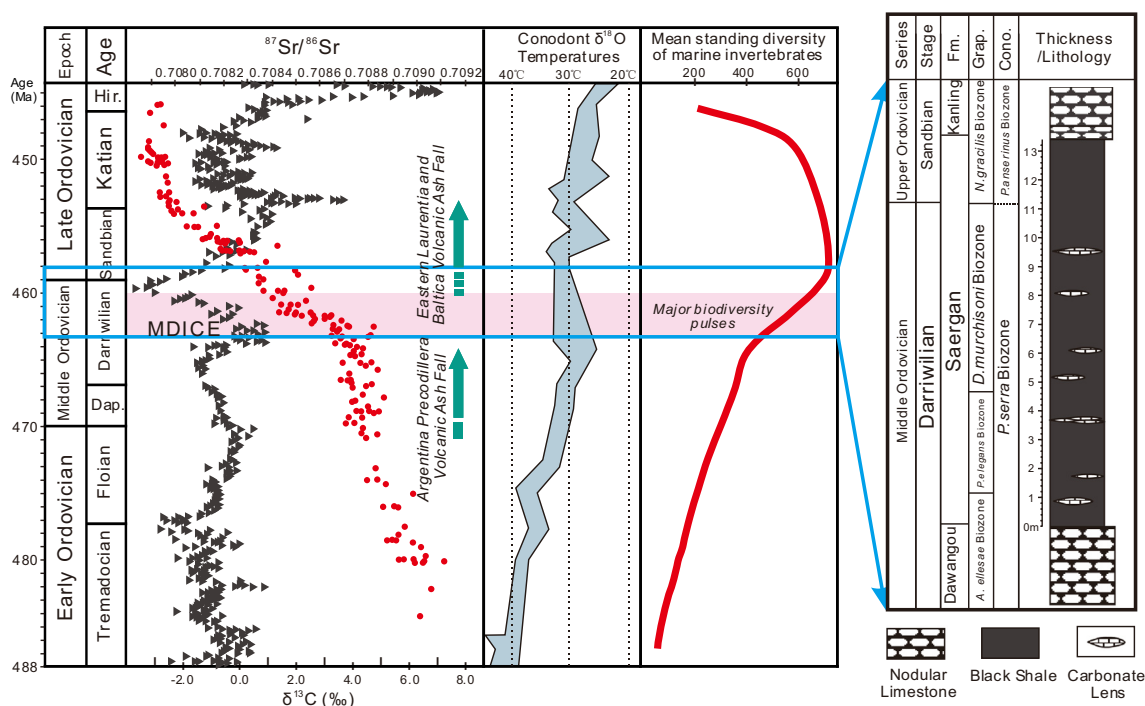
Fig. 8. The co-evolution of oceanic environment and life during the Ordovician Period. Composite global $^{87}Sr/^{86}Sr$ seawater curve in red circles (Young et al., 2009; McArthur et al., 2012), $\delta^{13}C$ seawater curve in black triangles (Saltzman and Thomas, 2012), palaeo-temperature inferred from conodont O-isotope data (Nardin et al., 2011), volcanic ash falling event from Huff (2008). Mean standing diversity of Ordovician marine invertebrates compiled by Kröger and Lintulaakso (2017). The right panel presents stratigraphic column of the Dawangou section in the Tarim Basin (MDICE = Middle Darriwilian $\delta^{13}C$ isotope excursion, Hir. = Hirnantian, Fm. = formation, Grap. = graptolite, Cono. = conodont). (For interpretation of the references to color in this figure legend, the reader is referred to the web version of this article.)

1970) rather than PAAS. However, the similarity in Al_2O_3 values between the average shale (16.7%; Wedepohl, 1970) and PAAS (18.9%; Taylor and McLennan, 1985), enrichment factors calculated for upwelling zones and COAE sediments (Brumsack, 2006) are comparable to the Saergan Formation (Fig. 10).

Significant enrichment of authigenic Mo is generally associated with the presence of H_2S (i.e., euxinic conditions), which would favor the transformation from stable molybdate to particle-reactive thiomolybdates (Helz et al., 1996; Tribovillard et al., 2012). Mo content in the Saergan Formation are not significantly enriched, indicating the absence of H_2S in the water column. V is commonly released from sediments deposited under low-oxygen (but still oxygenated) conditions and under normal bottom water oxygen levels where oxygen only penetrates a few millimeters into the sediment (Morford and Emerson, 1999). Yet in the absence of oxygen, the vanadate is reduced to the vanadyl form V(IV) (Emerson and Huested, 1991), which is highly surface-reactive and removed to the sediment (Wanty and Goldhaber, 1992; Zhang et al., 2016), resulting in V enrichment in sediments below an anoxic water column. In this context, the Saergan shales show negligible V enrichment overall, most likely having been deposited in a low-oxygen environment. In contrast to Mo and V, U is preferentially taken up by sediments in suboxic conditions prior to the onset of sulphate reduction that would promote authigenic Mo and V accumulation since U (VI) is reduced at the Fe(II)–Fe(III) redox boundary (McManus et al., 2005; Morford et al., 2005). In this light, enrichment of U relative to V and Mo in Phase 2 (Fig. 4) suggests a suboxic environment, which is consistent with the depletion of Fe and Mn (Fig. 10; Brumsack, 2006). In addition, the presences of benthic organisms (e.g., trilobites, Fig. 3B) and graptolites in the Saergan Formation (Chen et al., 2012; Bergström et al., 2017) further supports a suboxic environment as well (Cooper et al., 2012a).

5.4. Nutrient availability and organic matter enrichment

In general, enrichment of organic matters in sediments may be favored by high primary productivity and/or well preservation in the anoxic seawater (Tyson, 2005), which could be indicative of either coastal upwelling zones or Oceanic Anoxic Events (OAEs) (Demaison and Moore, 1980; Tyson, 2005; Jenkyns, 2010), respectively. Organic-rich shales (TOC: 0.54–4.79 wt%, Fig. 4; Table 1) of the Saergan Formation were likely deposited in a suboxic environment, which was not optimal for organic matter preservation (Tyson, 2005). This indicates high primary productivity (or organic exports) was likely crucial for organic accumulation/enrichment which could have been driven by coastal upwelling. In the Saergan Shale, nutrient elements such as P, Ni, Cu, and Zn show enrichment factors (EF_P, EF_{Ni}, EF_{Cu}, and EF_{Zn}) ranging between 0.9–8.1, 1.4–6.1, 2.4–8.5, and 1.3–10.9, respectively. This scenario agrees with geochemical features that are similar to those from the coastal upwelling zone (Fig. 10), which have also been reported in other continents during the Darriwilian (Pope and Steffen, 2003; Luan et al., 2018; Rasumussen and Stouge, 2018).

Traditionally, phosphorus and selected trace elements (e.g., Ni, Cu, Zn, Ba, Cr) are widely used to evaluate paleoproductivity (Algeo and Maynard, 2004; Piper and Perkins, 2004; Tribovillard et al., 2004, 2006; Schoepfer et al., 2015). These elements generally show distinctive distribution patterns in sediments deposited in coastal upwelling zones and silled anoxic marine basins (Fig. 10). In the Saergan Formation, enrichment factors of paleo-productivity (P, Ni, Cu, Zn, Ba, Cr) generally fall in the range of those from coastal upwelling zone sediments (Fig. 10). More importantly, elevated P and Ba contents (although fluctuating) in Phase 2 relative to Phase 1 and 3 (Fig. 4) demonstrate an increase in primary productivity, suggesting deposition in an upwelling zone where bio-limiting nutrients been pumped upward from deep cold waters (Mullins et al., 1985). In addition, climatic cooling starting in Phase 1, as evidenced by the CIA data (Fig. 4), could
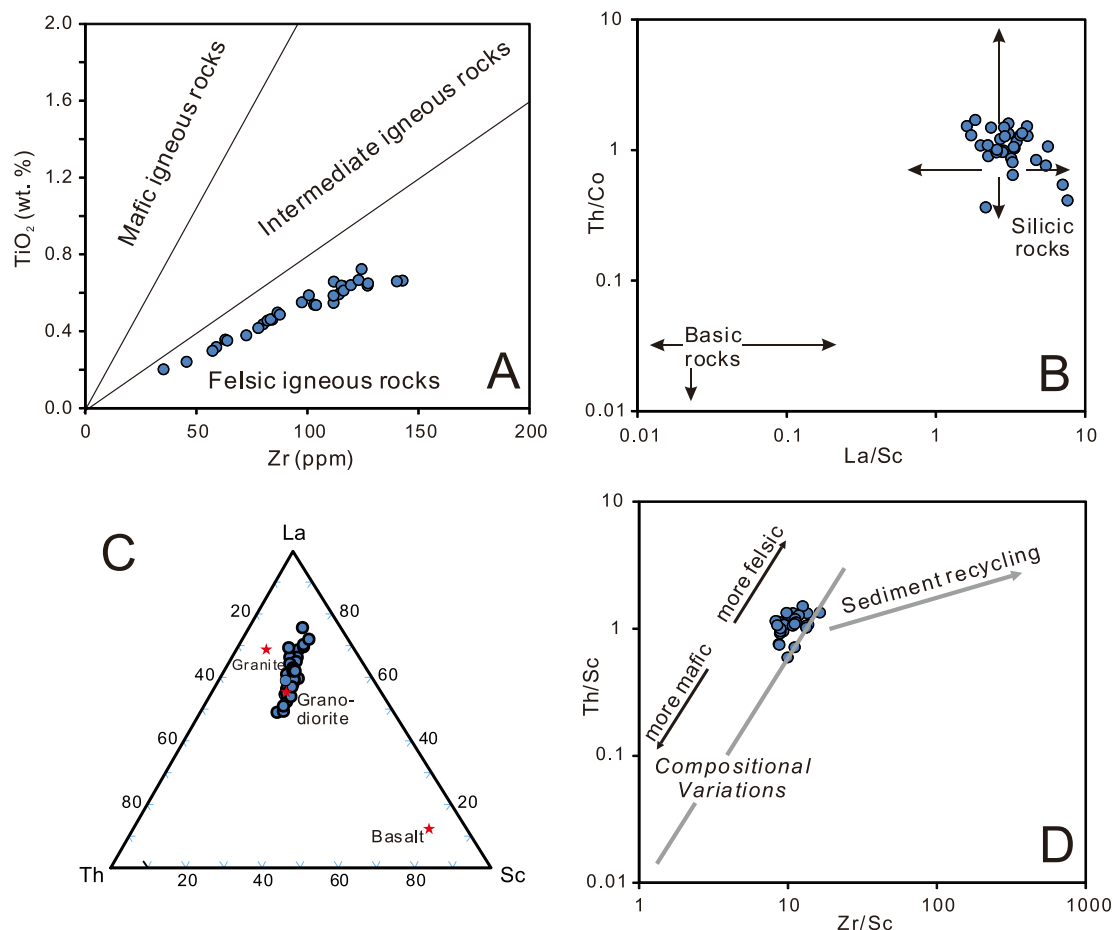
Fig. 9. Discrimination diagrams illustrating sedimentary provenance and transport cycles. A) TiO_2 versus Zr diagram. All samples are plot within the area of felsic igneous rock source (Hayashi et al., 1997). B) Th/Co versus La/Sc diagram (Cullers, 2002). All samples plot in the area representing silicic rocks. C) La–Th–Sc diagram (Cullers and Podkovyrov, 2000). Samples are plot close to granite and granodiorite. D) Th/Sc vs. Zr/Sc diagram (McLennan et al., 1993). Samples plot in the area with no sediment recycling.
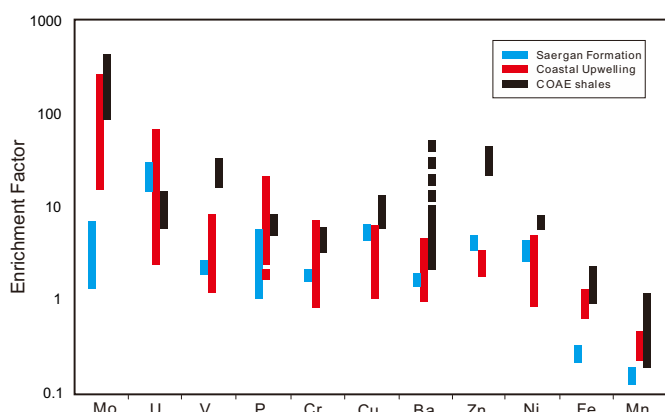
Fig. 10. Comparison of enrichment factors for selected trace elements in shales from the Saergan Formation at the Dawangou section (normalized to PAAS), coastal upwelling zones and Cretaceous Oceanic Anoxic Events (COAE) (Brumsack, 2006).

have also improved the ocean circulation to some extent, thereby enhancing the oceanic upwelling.

5.5. Environment implications during the major pulse of GOBE

The GOBE is a sum of diversification of multiple individual groups that show rapid increases during different intervals (Webby et al., 2004;

Servais and Harper, 2018). In the short time interval spanning from late Middle Ordovician to early Late Ordovician, level-bottom benthic and reef communities demonstrate a sharp increase of biodiversity at the global scale (Fig. 8; Harper, 2006). It is commonly suggested that such a large increase in biodiversity involved complex of geologic, geographic, climatic, and oceanographic factors (Webby et al., 2004; Servais et al., 2009, 2010; Zhang et al., 2010; Thompson et al., 2012; Edwards, 2018).

During the late Darriwilian age when the lower part of the Saergan Formation was deposited (Phase 1), intense volcanism evidenced by increasing Hg/TOC ratios (Fig. 4), and decreasing $\delta^{13}C$ (Albanesi et al., 2013; Sial et al., 2013b; Edwards et al., 2015) and $^{87}Sr/^{86}Sr$ ratios (Qing et al., 1998; Shields et al., 2003; Kah et al., 2016; Fig. 8), may have released significant greenhouse gases into the atmosphere and bio-limiting elements to the oceans and subsequently led to climate warming. In turn, this would have enhanced chemical weathering and riverine fluxes as evidenced by the high CIA values (Fig. 4). Subsequent decrease of volcanogenic greenhouse gases in response to waning volcanism and resultant CO_2 drawdown by silicate weathering could have collectively caused climate cooling, as shown by the episodic decreases in CIA values through late Phase 1 to Phase 3 (Fig. 4). Climatic cooling would have enhanced oceanic circulation, facilitating upwelling of nutrient-rich deepwaters to surface waters along the shelf margin (Fig. 11). In this scenario, the transition into a cooler climate and enhanced circulation of watermasses in the context of marine transgression (or highstand) may have increased habitable niche space in shallow water regime for benthic dwellers, accelerating their colonization and expansion of living space in the shallow marine regime,
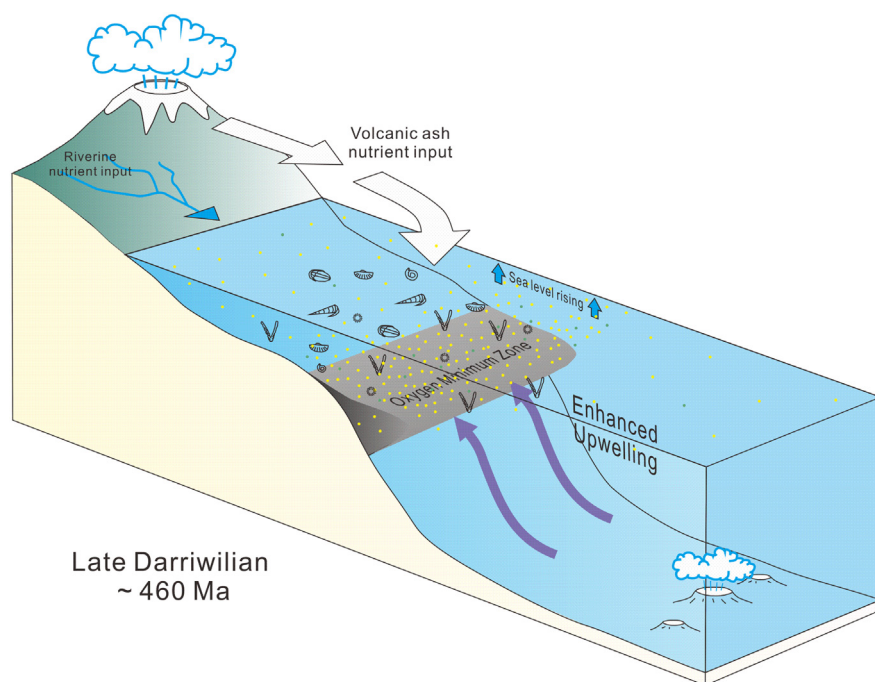
Fig. 11. Schematic model illustrating the co-evolution of volcanoes, climate and oceans during the Middle-Late Ordovician transition. In this scenario, sea level rise created more shelf habitats for marine organisms. Enhanced aeolian input and upwelling of waters delivered excessive amount of nutrients to the epicontinental surface sea water, which stimulating primary productivity (indicated by yellow and green dots), the formation of organic-rich black shale and a major pulse of the GOBE. (For interpretation of the references to color in this figure legend, the reader is referred to the web version of this article.)

thereby stimulating the great diversification of marine benthic fauna as that has been extensively documented as the GOBE.

6. Conclusions

The Mid-Upper Ordovician Saergan Formation from the Dawangou Section witnessed an episode of intensified, then attenuated volcanic activity from the late Darriwilian to the earliest Sandbian age. Enhanced volcanic activity could have greatly increased atmospheric greenhouse gas concentration and nutrient inputs, causing climate warming, enhanced chemical weathering and slowed oceanic circulation (or ocean stratification). Subsequent waning volcanism would reduce greenhouse gas venting, inducing climate cooling, thereby enhancing oceanic circulation and upwelling in the context of sea-level highstand. The transition into a cooler climate and ventilated ocean could have created a more habitable and expanded niche in the shallow-water regime, accelerating the colonization and diversification of the benthic dwellers. Our geochemical data from the Middle-Upper Ordovician Saergan Formation thus offer useful evidence for understanding of the life-environment co-evolution of the major pulse of the GOBE during the Middle-Late Ordovician transition.

Acknowledgments

References

Adrain, J.M., Edgecombe, G.D., Fortey, R.A., Hammer, Ø., Laurie, J.R., McCormick, T., Owen, A.W., Waisfeld, B.G., Webby, B.D., Westrop, S.R., Zhou, Z.-Y., 2004. Trilobites. In: Webby, B.D., Droser, M.L., Paris, F., Percival, I.G. (Eds.), The Great Ordovician Biodiversification Event. Columbia University Press, New York, pp. 231–254.

Albanesi, G.L., Bergström, S.M., Schmitz, B., Serra, F., Feltes, N.A., Voldman, G.G., Ortega, G., 2013. Darriwilian (Middle Ordovician) $\delta^{13}C_{carb}$ chemostratigraphy in the Precordillera of Argentina: documentation of the middle Darriwilian Isotope Carbon Excursion (MDICE) and its use for intercontinental correlation. Palaeogeogr. Palaeoclimatol. Palaeoecol. 389, 48–63.

Algeo, T.J., 1996. Geomagnetic polarity bias patterns through the Phanerozoic. J. Geophys. Res. Solid Earth 101, 2785–2814.

Algeo, T.J., Maynard, J.B., 2004. Trace-element behavior and redox facies in core shales of Upper Pennsylvanian Kansas-type cyclothems. Chem. Geol. 206, 289–318.

Algeo, T.J., Marenco, P.J., Saltzman, M.R., 2016. Co-evolution of oceans, climate, and the biosphere during the 'Ordovician Revolution': a review. Palaeogeogr. Palaeoclimatol. Palaeoecol. 458, 1–11.

Astini, R.A., Collo, G., Martina, F., 2007. Ordovician K-bentonites in the upper-plate active margin of Western Gondwana, (Famatina Ranges): stratigraphic and palaeogeographic significance. Gondwana Res. 11, 311–325.

Bahlburg, H., Dobrzinski, N., 2011. Chapter 6 a review of the Chemical Index of Alteration (CIA) and its application to the study of Neoproterozoic glacial deposits and climate transitions. Geol. Soc. Lond. Mem. 36, 81–92.

Barnes, C.R., 2004. Was there an Ordovician superplume event? In: Webby, B.D., Droser, M.L., Paris, F., Percival, I.G. (Eds.), The Great Ordovician Biodiversification Event. Columbia University Press, New York, pp. 77–80.

Beckmann, B., Flogel, S., Hofmann, P., Schulz, M., Wagner, T., 2005. Orbital forcing of Cretaceous river discharge in tropical Africa and ocean response. Nature 437, 241–244.

Bergström, S.M., Ferretti, A., 2017. Conodonts in Ordovician biostratigraphy. Lethaia 50, 424–439.

Bergström, S.M., Finney, S.C., Chen, X., Palsson, C., Wang, Z.-H., Grahn, Y., 2000. A Proposed Global Boundary Stratotype for the Base of the Upper Series of the Ordovician System: The Fågelsång Section, Scania, Southern Sweden. Episodes 23. pp. 102–109.

Bergström, S.M., Wang, Z., Goldman, D., 2017. Relations between Darriwilian and Sandbian conodont and graptolite biozones. In: Chen, X., Bergström, S.M., Finney, S.C., Zhang, Y., Fan, J., Chen, Q., Goldman, D., Wang, Z., Ma, X. (Eds.), Darriwilian to Sandbian (Ordovician) Graptolites From Northwest China. Elsevier, Amsterdam, Netherland, pp. 39–78.

Braddy, S., Tollerton, V.P., Racheboeuf, P.R., Schallreuter, R., 2004. Eurypterids, phyllocarids, and ostracodes. In: Webby, B.D., Droser, M.L., Paris, F., Percival, I.G. (Eds.), The Great Ordovician Biodiversification Event. Columbia University Press, New York, pp. 255–265.

Brumsack, H.J., 2006. The trace metal content of recent organic carbon-rich sediments: implications for Cretaceous black shale formation. Palaeogeogr. Palaeoclimatol. Palaeoecol. 232, 344–361.

Calvert, S.E., Pedersen, T.F., 1993. Geochemistry of recent oxic and anoxic marine sediments: implications for the geological record. Mar. Geol. 113, 67–88.

Charbonnier, G., Godet, A., Bodin, S., Adatte, T., Föllmi, K.B., 2018. Mercury anomalies, volcanic pulses, and drowning episodes along the northern Tethyan margin during the latest Hauterivian-earliest Aptian. Palaeogeogr. Palaeoclimatol. Palaeoecol. 505, 337–350.

Chen, X., 2017. A comment on the Saergan, Yingan and equivalent formations as potential source rocks for petroleum. In: Chen, X., Bergström, S.M., Finney, S.C., Zhang, Y., Fan, J., Chen, Q., Goldman, D., Wang, Z., Ma, X. (Eds.), Darriwilian to Sandbian (Ordovician) Graptolites From Northwest China. Elsevier, Amsterdam, Netherland, pp. 87–93.

Chen, X., Zhang, Y.-D., Bergström, S.M., Xu, H.-G., 2006. Upper Darriwilian graptolite and conodont zonation in the global stratotype section of the Darriwilian stage

(Ordovician) at Huangnitang, Changshan, Zhejiang, China. Palaeoworld 15, 150–170.

Chen, X., Zhang, Y., Li, Y., Fan, J., Tang, P., Chen, Q., Zhang, Y., 2012. Biostratigraphic correlation of the Ordovician black shales in Tarim Basin and its peripheral regions. Sci. China Earth Sci. 55, 1230–1237.

Chen, X., Zhang, Y., Wang, Z., Daniel, G., Bergström, S.M., Fan, J., Finney, S.C., Chen, Q., 2017. Biostratigraphy. In: Chen, X., Bergström, S.M., Finney, S.C., Zhang, Y., Fan, J., Chen, Q., Goldman, D., Wang, Z., Ma, X. (Eds.), Darriwilian to Sandbian (Ordovician) Graptolites From Northwest China. Elsevier, Amsterdam, Netherland, pp. 7–38.

Cocks, L.R.M., Torsvik, T.H., 2002. Earth geology from 500 to 400 million years ago: a faunal and palaeomagnetic review. J. Geol. Soc. Lond. 159, 631–644.

Condie, K.C., 1993. Chemical composition and evolution of the upper continental crust: contrasting results from surface samples and shales. Chem. Geol. 104, 1–37.

Cooper, R.A., Rigby, S., Loydell, D.K., Bates, D.E.B., 2012a. Palaeoecology of the Graptoloidea. Earth Sci. Rev. 112, 23–41.

Cooper, R.A., Sadler, P.M., Hammer, O., Gradstein, F.M., 2012b. The Ordovician period. In: The Geologic Time Scale, pp. 489–523.

Cullers, R.L., 2002. Implications of elemental concentrations for provenance, redox conditions, and metamorphic studies of shales and limestones near Pueblo, CO, USA. Chem. Geol. 191, 305–327.

Cullers, R.L., Podkovyrov, V.N., 2000. Geochemistry of the Mesoproterozoic Lakhanda shales in southeastern Yakutia, Russia: implications for mineralogical and provenance control, and recycling. Precambrian Res. 104, 77–93.

Demaison, G.J., Moore, G.T., 1980. Anoxic environments and oil source bed genesis. Org. Geochem. 2, 9–31.

Edwards, C.T., 2018. Links between early Paleozoic oxygenation and the Great Ordovician Biodiversification Event (GOBE): a review. Palaeoworld. https://doi.org/10.1016/j.palwor.2018.08.006. In press.

Edwards, C.T., Saltzman, M.R., 2016. Paired carbon isotopic analysis of Ordovician bulk carbonate ($\delta^{13}C_{carb}$) and organic matter ($\delta^{13}C_{org}$) spanning the Great Ordovician Biodiversification Event. Palaeogeogr. Palaeoclimatol. Palaeoecol. 458, 102–117.

Edwards, C.T., Saltzman, M.R., Leslie, S.A., Bergström, S.M., Sedlacek, A.R.C., Howard, A., Bauer, J.A., Sweet, W.C., Young, S.A., 2015. Strontium isotope ($^{87}Sr/^{86}Sr$) stratigraphy of Ordovician bulk carbonate: implications for preservation of primary seawater values. Geol. Soc. Am. Bull. 127, 1275–1289.

Emerson, S.R., Huested, S.S., 1991. Ocean anoxia and the concentrations of molybdenum and vanadium in seawater. Mar. Chem. 34, 177–196.

Fagel, N., 2007. Chapter four clay minerals, deep circulation and climate. In: Proxies in Late Cenozoic Paleoceanography, pp. 139–184.

Fedo, C.M., Nesbitt, H.W., Young, G.M., 1995. Unraveling the effects of potassium metasomatism in sedimentary rocks and paleosols, with implications for paleo-weathering conditions and provenance. Geology 23, 921–924.

Finnegan, S., Heim, N.A., Peters, S.E., Fischer, W.W., 2012. Climate change and the selective signature of the Late Ordovician mass extinction. Proc. Natl. Acad. Sci. U. S. A. 109, 6829–6834.

Font, E., Adatte, T., Sial, A.N., Drude de Lacerda, L., Keller, G., Punekar, J., 2016. Mercury anomaly, Deccan volcanism, and the end-Cretaceous mass extinction. Geology 44, 171–174.

Francois, R., 1988. A study on the regulation of the concentrations of some trace metals (Rb, Sr, Zn, Pb, Cu, V, Cr, Ni, Mn and Mo) in Saanich Inlet Sediments, British Columbia, Canada. Mar. Geol. 83, 285–308.

Gao, Z., Zhang, S., Li, J., Zhang, B., Gu, Q., Lu, Y., 2010. Distribution and sedimentary environments of Salgan and Yingan shales of the Middle-Upper Ordovician in western Tarim Basin. J. Palaeogeogr. 12, 599–608 (in Chinese).

Garver, J.I., Royce, T.A., 1996. Chromium and nickel in shale of the taconic foreland: a case study for the provenance of fine-grained sediments with an ultramafic source. SEPM J. Sediment. Res. 66, 100–106.

Gong, Q., Wang, X., Zhao, L., Grasby, S.E., Chen, Z.Q., Zhang, L., Li, Y., Cao, L., Li, Z., 2017. Mercury spikes suggest volcanic driver of the Ordovician-Silurian mass extinction. Sci. Rep. 7, 5304.

Graham, S.A., Brassell, S.C., Carroll, A.R., Xiao, X., Demaison, G., McKnight, C.L., Liang, Y., Chu, J., Hendrix, M.S., 1990. Characteristics of selected petroleum source rocks, Xianjiang Uygur Autonomous Region, NW China. AAPG Bull. 74, 493–512.

Grasby, S.E., Sanei, H., Beauchamp, B., Chen, Z., 2013. Mercury deposition through the Permo–Triassic biotic crisis. Chem. Geol. 351, 209–216.

Gustin, M.S., Lindberg, S.E., Weisberg, P.J., 2008. An update on the natural sources and sinks of atmospheric mercury. Appl. Geochem. 23, 482–493.

Haq, B.U., Schutter, S.R., 2008. A chronology of Paleozoic sea-level changes. Science 322, 64–68.

Harper, D.A.T., 2006. The Ordovician biodiversification: setting an agenda for marine life. Palaeogeogr. Palaeoclimatol. Palaeoecol. 232, 148–166.

Hayashi, K.-I., Fujisawa, H., Holland, H.D., Ohmoto, H., 1997. Geochemistry of ~ 1.9 Ga sedimentary rocks from northeastern Labrador, Canada. Geochim. Cosmochim. Acta 61, 4115–4137.

Helz, G.R., Miller, C.V., Charnock, J.M., Mosselmans, J.F.W., Pattrick, R.A.D., Garner, C.D., Vaughan, D.J., 1996. Mechanism of molybdenum removal from the sea and its concentration in black shales: EXAFS evidence. Geochim. Cosmochim. Acta 60, 3631–3642.

Huff, W.D., 2008. Ordovician K-bentonites: issues in interpreting and correlating ancient tephras. Quat. Int. 178, 276–287.

Jenkyns, H.C., 2010. Geochemistry of oceanic anoxic events. Geochem. Geophys. Geosyst. 11, Q030r04.

Jia, C., Wang, L., Wei, G., Chen, H., Jia, D., Guo, Z., Xiao, A., 2004. Tectonic Evolution and Continental Dynamics of Tarim Basin. Petroleum Industry Press, Beijing, pp. 1–165 (in Chinese).

Jones, M.T., Gislason, S.R., 2008. Rapid releases of metal salts and nutrients following the deposition of volcanic ash into aqueous environments. Geochim. Cosmochim. Acta 72, 3661–3680.

Jones, D.S., Martini, A.M., Fike, D.A., Kaiho, K., 2017. A volcanic trigger for the Late Ordovician mass extinction? Mercury data from south China and Laurentia. Geology 45, 631–634.

Kah, L.C., Thompson, C.K., Henderson, M.A., Zhan, R., 2016. Behavior of marine sulfur in the Ordovician. Palaeogeogr. Palaeoclimatol. Palaeoecol. 458, 133–153.

Kolata, D.R., Huff, W.D., Bergström, S.M., 1998. Nature and regional significance of unconformities associated with the Middle Ordovician Hagan K-bentonite complex in the North American midcontinent. Geol. Soc. Am. Bull. 110, 723–739.

Kröger, B., Lintulaakso, K., 2017. RNames, a stratigraphical database designed for the statistical analysis of fossil occurrences – the Ordovician diversification as a case study. Palaeontol. Electron. 20, 1–12.

Legget, J.K., McKerrow, W.S., Cocks, L.R.M., Richards, R.B., 1981. Periodicity in the early Palaeozoic marine realm. J. Geol. Soc. 138, 167–176.

Lev, S.M., McLennan, S.M., Meyers, W.J., Hanson, G.N., 1998. A petrographic approach for evaluating trace-element mobility in a black shale. J. Sediment. Res. 68, 970–980.

Lin, C., Yang, H., Liu, J., Rui, Z., Cai, Z., Zhu, Y., 2012. Distribution and erosion of the Paleozoic tectonic unconformities in the Tarim Basin, Northwest China: significance for the evolution of paleo-uplifts and tectonic geography during deformation. J. Asian Earth Sci. 46, 1–19.

Little, S.H., Vance, D., Lyons, T.W., McManus, J., 2015. Controls on trace metal authigenic enrichment in reducing sediment: insights from modern oxygen-deficient settings. Am. J. Sci. 315, 77–119.

Luan, X., Brett, C.E., Zhan, R., Jin, J., Wu, R., Gong, F., 2018. Middle-Late Ordovician iron-rich nodules on Yangtze Platform, South China, and their palaeoenvironmental implications. Lethaia 51, 523–537.

Ma, X., Wang, Z.-H., Zhang, Y.-D., Song, Y.-Y., Fang, X., 2015. Carbon isotope records of the Middle–Upper Ordovician transition in Yichang area, South China. Palaeoworld 24, 136–148.

McArthur, J.M., Howarth, R.J., Shields, G.A., 2012. Strontium isotope stratigraphy. In: The Geologic Time Scale, pp. 127–144.

McLennan, S.M., 1993. Weathering and global denudation. J. Geol. 101, 295–303.

McLennan, S.M., 2001. Relationships between the trace element composition of sedimentary rocks and upper continental crus. Geochem. Geophys. Geosyst. 2, 2000GC000109.

McLennan, S.M., Taylor, S.R., 1991. Sedimentary rocks and crustal evolution: tectonic setting and secular trends. J. Geol. 99, 1–21.

McLennan, S.M., McDaniel, D.K., Hanson, G.N., 1993. Geochemical Approaches to Sedimentation, Provenance, and Tectonics. Geological Society of America Special Paper, Boulder, Colorado, pp. 21–40.

McManus, J., Berelson, W.M., Klinkhammer, G.P., Hammond, D.E., Holm, C., 2005. Authigenic uranium: relationship to oxygen penetration depth and organic carbon rain. Geochim. Cosmochim. Acta 69, 95–108.

Meyer, K.M., Kump, L.R., 2008. Oceanic euxinia in earth history: causes and consequences. Annu. Rev. Earth Planet. Sci. 36, 251–288.

Min, K., Renne, P.R., Huff, W.D., 2001. $^{40}Ar/^{39}Ar$ dating of Ordovician K-bentonites in Laurentia and Baltoscandia. Earth Planet. Sci. Lett. 185, 121–134.

Morford, J.L., Emerson, S., 1999. The geochemistry of redox sensitive trace metals in sediments. Geochim. Cosmochim. Acta 63, 1735–1750.

Morford, J.L., Emerson, S.R., Breckel, E.J., Kim, S.H., 2005. Diagenesis of oxyanions (V, U, Re, and Mo) in pore waters and sediments from a continental margin. Geochim. Cosmochim. Acta 69, 5021–5032.

Mullins, H.T., Thompson, J.B., McDougall, K., Vercoutere, T.L., 1985. Oxygen-minimum zone edge effects: evidence from the central California coastal upwelling system. Geology 13, 491–494.

Munnecke, A., Zhang, Y., Liu, X., Cheng, J., 2011. Stable carbon isotope stratigraphy in the Ordovician of South China. Palaeogeogr. Palaeoclimatol. Palaeoecol. 307, 17–43.

Nardin, E., Godderis, Y., Donnadieu, Y., Le Hir, G., Blakey, R.C., Puceat, E., Aretz, M., 2011. Modeling the early Paleozoic long-term climatic trend. Geol. Soc. Am. Bull. 123, 1181–1192.

Nascimento-Silva, M.V., Sial, A.N., Ferreira, V.P., Neumann, V.H., Barbosa, J.A., Pimentel, M.M., de Lacerda, L.D., 2011. Cretaceous-Paleogene transition at the Paraíba Basin, Northeastern, Brazil: carbon-isotope and mercury subsurface stratigraphies. J. S. Am. Earth Sci. 32, 379–392.

Nesbitt, H.W., Young, G.M., 1982. Early Proterozoic climates and plate motions inferred from major element chemistry of lutites. Nature 299, 715–716.

Nesbitt, H.W., Young, G.M., 1989. Formation and diagenesis of weathering profiles. J. Geol. 97, 129–147.

Panahi, A., Young, G.M., Rainbird, R.H., 2000. Behavior of major and trace elements (including REE) during Paleoproterozoic pedogenesis and diagenetic alteration of an Archean granite near Ville Marie, Québec, Canada. Geochim. Cosmochim. Acta 64, 2199–2220.

Percival, L.M.E., Witt, M.L.I., Mather, T.A., Hermoso, M., Jenkyns, H.C., Hesselbo, S.P., Al-Suwaidi, A.H., Storm, M.S., Xu, W., Ruhl, M., 2015. Globally enhanced mercury deposition during the end-Pliensbachian extinction and Toarcian OAE: a link to the Karoo–Ferrar Large Igneous Province. Earth Planet. Sci. Lett. 428, 267–280.

Percival, L.M.E., Jenkyns, H.C., Mather, T.A., Dickson, A.J., Batenburg, S.J., Ruhl, M., Hesselbo, S.P., Barclay, R.S., Jarvis, I.A.N., 2018. Large igneous province volcanism mercury cycle Oceanic Anoxic Event 2 end-Cretaceous Mesozoic events. Am. J. Sci. 318, 1–62.

Piper, D.Z., Calvert, S.E., 2009. A marine biogeochemical perspective on black shale deposition. Earth Sci. Rev. 95, 63–96.

Piper, D.Z., Perkins, R.B., 2004. A modern vs. Permian black shale—the hydrography, primary productivity, and water-column chemistry of deposition. Chem. Geol. 206, 177–197.

Pirrone, N., Cinnirella, S., Feng, X., Finkelman, R.B., Friedli, H.R., Leaner, J., Mason, R., Mukherjee, A.B., Stracher, G.B., Streets, D.G., Telmer, K., 2010. Global mercury emissions to the atmosphere from anthropogenic and natural sources. Atmos. Chem. Phys. 10, 5951–5964.

Pohl, A., Donnadieu, Y., Le Hir, G., Ladant, J.-B., Dumas, C., Alvarez-Solas, J., Vandenbroucke, T.R.A., 2016. Glacial onset predated Late Ordovician climate cooling. Paleoceanography 31, 800–821.

Pope, M.C., Steffen, J.B., 2003. Widespread, prolonged late Middle to Late Ordovician upwelling in North America: a proxy record of glaciation? Geology 31, 63–66.

Pyle, D.M., Mather, T.A., 2003. The importance of volcanic emissions for the global atmospheric mercury cycle. Atmos. Environ. 37, 5115–5124.

Qi, L., Hu, J., Gregoire, D.C., 2000. Determination of trace elements in granites by inductively coupled plasma mass spectrometry. Talanta 51, 507–513.

Qing, H., Barnes, C.R., Buhl, D., Veizer, J., 1998. The strontium isotopic composition of Ordovician and Silurian brachiopods and conodonts Relationships to geological events and implications for coeval seawater. Geochim. Cosmochim. Acta 62, 1721–1733.

Racki, G., Rakociński, M., Marynowski, L., Wignall, P.B., 2018. Mercury enrichments and the Frasnian-Famennian biotic crisis: a volcanic trigger proved? Geology 46, 543–546.

Rasmussen, C.M., Ullmann, C.V., Jakobsen, K.G., Lindskog, A., Hansen, J., Hansen, T., Eriksson, M.E., Dronov, A., Frei, R., Korte, C., Nielsen, A.T., Harper, D.A., 2016. Onset of main Phanerozoic marine radiation sparked by emerging Mid Ordovician icehouse. Sci. Rep. 6, 18884.

Rasumussen, J.A., Stouge, S., 2018. Baltoscandian conodont biofacies fluctuations and their link to Middle Ordovician (Darriwilian) global cooling. Palaeontology 61 (3), 391–416.

Rieu, R., Allen, P.A., Plötze, M., Pettke, T., 2007. Climatic cycles during a Neoproterozoic "snowball" glacial epoch. Geology 35, 299–302.

Robbins, L.J., Lalonde, S.V., Planavsky, N.J., Partin, C.A., Reinhard, C.T., Kendall, B., Scott, C., Hardisty, D.S., Gill, B.C., Alessi, D.S., Dupont, C.L., Saito, M.A., Crowe, S.A., Poulton, S.W., Bekker, A., Lyons, T.W., Konhauser, K.O., 2016. Trace elements at the intersection of marine biological and geochemical evolution. Earth Sci. Rev. 163, 323–348.

Sabatino, N., Ferraro, S., Coccioni, R., Bonsignore, M., Del Core, M., Tancredi, V., Sprovieri, M., 2018. Mercury anomalies in upper Aptian-lower Albian sediments from the Tethys realm. Palaeogeogr. Palaeoclimatol. Palaeoecol. 495, 163–170.

Saltzman, M.R., Edwards, C.T., 2017. Gradients in the carbon isotopic composition of Ordovician shallow water carbonates: a potential pitfall in estimates of ancient CO_2 and O_2. Earth Planet. Sci. Lett. 464, 46–54.

Saltzman, M.R., Thomas, E., 2012. Carbon Isotope Stratigraphy. The Geologic Time Scale 207–232.

Sanei, H., Grasby, S.E., Beauchamp, B., 2012. Latest Permian mercury anomalies. Geology 40, 63–66.

Scaife, J.D., Ruhl, M., Dickson, A.J., Mather, T.A., Jenkyns, H.C., Percival, L.M.E., Hesselbo, S.P., Cartwright, J., Eldrett, J.S., Bergman, S.C., Minisini, D., 2017. Sedimentary mercury enrichments as a marker for submarine large igneous province volcanism? Evidence from the Mid-Cenomanian Event and Oceanic Anoxic Event 2 (Late Cretaceous). Geochem. Geophys. Geosyst. 18, 4253–4275.

Schmitz, B., Bergstrom, S.M., Xiaofeng, W., 2010. The middle Darriwilian (Ordovician) δ^{13}C excursion (MDICE) discovered in the Yangtze Platform succession in China: implications of its first recorded occurrences outside Baltoscandia. J. Geol. Soc. 167, 249–259.

Schoepfer, S.D., Shen, J., Wei, H., Tyson, R.V., Ingall, E., Algeo, T.J., 2015. Total organic carbon, organic phosphorus, and biogenic barium fluxes as proxies for paleomarine productivity. Earth Sci. Rev. 149, 23–52.

Sell, B.K., Samson, S.D., Mitchell, C.E., McLaughlin, P.I., Koenig, A.E., Leslie, S.A., 2015. Stratigraphic correlations using trace elements in apatite from Late Ordovician (Sandbian-Katian) K-bentonites of eastern North America. Geol. Soc. Am. Bull. 127, 1259–1274.

Sepkoski Jr., J.J., 1981. A factor analytical description of the Phanerozoic marine fossil. Paleobiology 7, 36–53.

Servais, T., Harper, D.A.T., 2018. The Great Ordovician Biodiversification Event (GOBE): definition, concept and duration. Lethaia 51 (2), 151–164.

Servais, T., Harper, D.A.T., Munnecke, A., Owen, A.W., Sheehan, P.M., 2009. Understanding the Great Ordovician Biodiversification Event (GOBE): influences of paleogeography, paleoclimate, or paleoecology. GSA Today 19, 4–10.

Servais, T., Owen, A.W., Harper, D.A.T., Kröger, B., Munnecke, A., 2010. The Great Ordovician Biodiversification Event (GOBE): the palaeoecological dimension. Palaeogeogr. Palaeoclimatol. Palaeoecol. 294, 99–119.

Shields, G.A., Carden, G.A.F., Veizer, J., Meidla, T., Rong, J.-Y., Li, R.-Y., 2003. Sr, C, and O isotope geochemistry of Ordovician brachiopods: a major isotopic event around the Middle-Late Ordovician transition. Geochim. Cosmochim. Acta 67, 2005–2025.

Sial, A.N., Lacerda, L.D., Ferreira, V.P., Frei, R., Marquillas, R.A., Barbosa, J.A., Gaucher, C., Windmöller, C.C., Pereira, N.S., 2013a. Mercury as a proxy for volcanic activity during extreme environmental turnover: the Cretaceous–Paleogene transition. Palaeogeogr. Palaeoclimatol. Palaeoecol. 387, 153–164.

Sial, A.N., Peralta, S., Gaucher, C., Toselli, A.J., Ferreira, V.P., Frei, R., Parada, M.A., Pimentel, M.M., Silva Pereira, N., 2013b. High-resolution stable isotope stratigraphy of the upper Cambrian and Ordovician in the Argentine Precordillera: carbon isotope excursions and correlations. Gondwana Res. 24, 330–348.

Smith, M.E., Singer, B.S., Simo, T., 2011. A time like our own? Radioisotopic calibration of the Ordovician greenhouse to icehouse transition. Earth Planet. Sci. Lett. 311, 364–374.

Strother, P.K., Al-Hajri, S., Traverse, A., 1996. New evidence for land plants from the lower Middle Ordovician of Saudi Arabia. Geology 24, 55–58.

Taylor, S.R., McLennan, S.M., 1985. The Continental Crust: Its Composition and Evolution. Blackwell Scientific Publications, Oxford, pp. 312.

Thibodeau, A.M., Ritterbush, K., Yager, J.A., West, A.J., Ibarra, Y., Bottjer, D.J., Berelson, W.M., Bergquist, B.A., Corsetti, F.A., 2016. Mercury anomalies and the timing of biotic recovery following the end-Triassic mass extinction. Nat. Commun. 7, 11147.

Thompson, C.K., Kah, L.C., Astini, R., Bowring, S.A., Buchwaldt, R., 2012. Bentonite geochronology, marine geochemistry, and the Great Ordovician Biodiversification Event (GOBE). Palaeogeogr. Palaeoclimatol. Palaeoecol. 321-322, 88–101.

Torsvik, T.H., Cocks, L.R.M., 2013. Chapter 2 New global palaeogeographical reconstructions for the Early Palaeozoic and their generation. Geol. Soc. Lond. Mem. 38, 5–24.

Tribovillard, N., Trentesaux, A., Ramdani, A., Baudin, F., Riboulleau, A., 2004. Controls on organic accumulation in late Jurassic shales of northwestern Europe as inferred from trace-metal geochemistry. Bull. Soc. Geol. Fr. 175, 491–506.

Tribovillard, N., Algeo, T.J., Lyons, T., Riboulleau, A., 2006. Trace metals as paleoredox and paleoproductivity proxies: an update. Chem. Geol. 232, 12–32.

Tribovillard, N., Algeo, T.J., Baudin, F., Riboulleau, A., 2012. Analysis of marine environmental conditions based on molybdenum-uranium covariation - applications to Mesozoic paleoceanography. Chem. Geol. 324-325, 46–58.

Trotter, J.A., Williams, I.S., Barnes, C.R., Lecuyer, C., Nicoll, R.S., 2008. Did cooling oceans trigger Ordovician Biodiversification? Evidence from conodont thermometry. Science 321, 550–554.

Tyson, R.V., 2005. The "productivity versus preservation" controversy: cause, flaw, and resolution. SEPM Spec. Publ. 82, 17–33.

Vandenbroucke, T.R.A., Armstrong, H.A., Williams, M., Paris, F., Sabbe, K., Zalasiewicz, J.A., Nõlvak, J., Verniers, J., 2010. Epipelagic chitinozoan biotopes map a steep latitudinal temperature gradient for earliest Late Ordovician seas: implications for a cooling Late Ordovician climate. Palaeogeogr. Palaeoclimatol. Palaeoecol. 294, 202–219.

Vaughan, A.P.M., Scarrow, J.H., 2003. Ophiolite obduction pulses as a proxy indicator of superplume events? Earth Planet. Sci. Lett. 213, 407–416.

Wang, X., Cawood, P.A., Zhao, H., Zhao, L., Grasby, S.E., Chen, Z.-Q., Wignall, P.B., Lv, Z., Han, C., 2018. Mercury anomalies across the end Permian mass extinction in South China from shallow and deep water depositional environments. Earth Planet. Sci. Lett. 496, 159–167.

Wanty, R.B., Goldhaber, M.B., 1992. Thermodynamics and kinetics of reactions involving vanadium in natural systems: accumulation of vanadium in sedimentary rocks. Geochim. Cosmochim. Acta 56, 1471–1483.

Webby, B.D., Paris, F., Droser, M.L., Percival, I.G., 2004. The Great Ordovician Biodiversification Event. Columbia University Press, New York, pp. 2.

Wedepohl, K.H., 1970. Geochemische Daten von sedimentaren Karbonaten und Karbonatgesteinen in ihrem faziellen und petrographischen Aussgewert. Verh. Geol. Bundesanst. 4, 692–705 (in German).

Xu, Z., Li, S., Yang, J., Yang, J., He, B., Li, H., Lin, C., Cai, Z., 2011. Paleo-Asian and Tethyan tectonic systems with docking the Tarim block. Acta Petrol. Sin. 27, 1–22.

Yarincik, K.M., Murray, R.W., Peterson, L.C., 2000. Climatically sensitive eolian and hemipelagic deposition in the Cariaco Basin, Venezuela, over the past 578,000 years: results from Al/Ti and K/Al. Paleoceanography 15, 210–228.

Young, G.M., Nesbitt, H.W., 1999. Paleoclimatology and provenance of the glaciogenic Gowganda Formation (Paleoproterozoic), Ontario, Canada: a chemostratigraphic approach. Geology 111, 264–274.

Young, S.A., Saltzman, M.R., Foland, K.A., Linder, J.S., Kump, L.R., 2009. A major drop in seawater ^{87}Sr/^{86}Sr during the Middle Ordovician (Darriwilian): links to volcanism and climate? Geology 37, 951–954.

Young, S.A., Gill, B.C., Edwards, C.T., Saltzman, M.R., Leslie, S.A., 2016. Middle–Late Ordovician (Darriwilian–Sandbian) decoupling of global sulfur and carbon cycles: isotopic evidence from eastern and southern Laurentia. Palaeogeogr. Palaeoclimatol. Palaeoecol. 458, 118–132.

Zhang, Y., Munnecke, A., 2016. Ordovician stable carbon isotope stratigraphy in the Tarim Basin, NW China. Palaeogeogr. Palaeoclimatol. Palaeoecol. 458, 154–175.

Zhang, T., Shen, Y., Algeo, T.J., 2010. High-resolution carbon isotopic records from the Ordovician of South China: links to climatic cooling and the Great Ordovician Biodiversification Event (GOBE). Palaeogeogr. Palaeoclimatol. Palaeoecol. 289, 102–112.

Zhang, S., Wang, X., Wang, H., Bjerrum, C.J., Hammarlund, E.U., Costa, M.M., Connelly, J.N., Zhang, B., Su, J., Canfield, D.E., 2016. Sufficient oxygen for animal respiration 1,400 million years ago. Proc. Natl. Acad. Sci. U. S. A. 113, 1731–1736.

Zhao, Z., Wang, J., Wang, P., 2017. Carbon and oxygen isotope variation and its implication for marine sequence: a case study of Ordovician in Tarim Basin. Pet. Res. 2, 281–290.

Zhen, Y.Y., Wang, Z., Zhang, Y., Bergström, S.M., Percival, I.G., Cheng, J., 2011. Middle to Late Ordovician (Darriwilian-Sandbian) conodonts from the Dawangou section, Kalpin area of the Tarim Basin, northwestern China. Rec. Aust. Mus. 63, 203–266.

Zhong, Y., Wu, H., Zhang, Y., Zhang, S., Yang, T., Li, H., Cao, L., 2018. Astronomical calibration of the Middle Ordovician of the Yangtze Block, South China. Palaeogeogr. Palaeoclimatol. Palaeoecol. 505, 86–99.